RIOJA. A Clumpy Galaxy Assembly at Redshift 6.81 Revealed by JWST

Citation for the original published paper (version of record):
Mawatari, K., Costantin, L., Usui, M. et al (2026). RIOJA. A Clumpy Galaxy Assembly at Redshift 6.81 Revealed by JWST. Astrophysical Journal, 998(1). http://dx.doi.org/10.3847/1538-4357/ae3151

The Astrophysical Journal, 998:119 (21pp), 2026 February 10 https://doi.org/10.3847/1538-4357/ae3151

RIOJA. A Clumpy Galaxy Assembly at Redshift 6.81 Revealed by JWST

Ken Mawatari[1,2,3,4], Luca Costantin[5], Mitsutaka Usui[3], Takuya Hashimoto[3,4], Javier Álvarez-Márquez[5], Yuma Sugahara[1,2], Luis Colina[5], Akio K. Inoue[1,2], Wataru Osone[3], Santiago Arribas[5], Rui Marques-Chaves[6], Yurina Nakazato[7,8], Masato Hagimoto[9], Takeshi Hashigaya[10], Daniel Ceverino[11,12], Naoki Yoshida[8,13,14], Tom J. L. C. Bakx[9,15,16], Yoshinobu Fudamoto[17], Alejandro Crespo Gómez[18], Hiroshi Matsuo[16,19], Miguel Pereira-Santaella[20], Carmen Blanco-Prieto[5], Yi W. Ren[2], and Yoichi Tamura[9]

[1] Waseda Research Institute for Science and Engineering, Faculty of Science and Engineering, Waseda University, 3-4-1 Okubo, Shinjuku, Tokyo 169-8555, Japan; mawatari@aoni.waseda.jp
[2] Department of Pure and Applied Physics, School of Advanced Science and Engineering, Faculty of Science and Engineering, Waseda University, 3-4-1 Okubo, Shinjuku, Tokyo 169-8555, Japan
[3] Division of Physics, Faculty of Pure and Applied Sciences, University of Tsukuba, Tsukuba, Ibaraki 305-8571, Japan
[4] Tomonaga Center for the History of the Universe (TCHoU), Faculty of Pure and Applied Sciences, University of Tsukuba, Tsukuba, Ibaraki 305-8571, Japan
[5] Centro de Astrobiología (CAB), CSIC-INTA, Ctra. de Ajalvir km 4, Torrejón de Ardoz, E-28850, Madrid, Spain
[6] Geneva Observatory, Department of Astronomy, University of Geneva, Chemin Pegasi 51, CH-1290 Versoix, Switzerland
[7] Center for Computational Astrophysics, Flatiron Institute, 162 5th Avenue, New York, NY, 10010, USA
[8] Department of Physics, The University of Tokyo, 7-3-1 Hongo, Bunkyo, Tokyo 113-0033, Japan
[9] Department of Physics, Graduate School of Science, Nagoya University, Nagoya, Aichi 464-8602, Japan
[10] Department of Astronomy, Kyoto University Sakyo-ku, Kyoto 606-8502, Japan
[11] Universidad Autonoma de Madrid, Ciudad Universitaria de Cantoblanco, E-28049 Madrid, Spain
[12] CIAFF, Facultad de Ciencias, Universidad Autonoma de Madrid, E-28049 Madrid, Spain
[13] Kavli Institute for the Physics and Mathematics of the Universe (WPI), UT Institute for Advanced Study, The University of Tokyo, Kashiwa, Chiba 277-8583, Japan
[14] Research Center for the Early Universe, School of Science, The University of Tokyo, 7-3-1 Hongo, Bunkyo, Tokyo 113-0033, Japan
[15] Department of Space, Earth, & Environment, Chalmers University of Technology, Chalmersplatsen 4 412 96 Gothenburg, Sweden
[16] National Astronomical Observatory of Japan, 2-21-1, Osawa, Mitaka, Tokyo, Japan
[17] Center for Frontier Science, Chiba University, 1-33 Yayoi-cho, Inage-ku, Chiba 263-8522, Japan
[18] Space Telescope Science Institute (STScI), 3700 San Martin Drive, Baltimore, MD 21218, USA
[19] Graduate University for Advanced Studies (SOKENDAI), 2-21-1 Osawa, Mitaka, Tokyo 181-8588, Japan
[20] Instituto de Física Fundamental (IFF), CSIC, Serrano 123, E-28006, Madrid, Spain

Received 2025 July 2; revised 2025 December 17; accepted 2025 December 22; published 2026 February 5

Abstract

Spatially resolved multiwavelength analysis is essential to study galaxy formation and evolution. A UV-bright galaxy COS-2987030247 at $z = 6.81$ is one of the Rosetta Stones in the epoch of reionization for which JWST NIRSpec Integral Field Spectroscopy, NIRCam imaging, and Atacama Large Millimeter/submillimeter Array data are available thanks to the RIOJA program. We identified the rest-frame optical emission lines from the ionized hydrogen, oxygen, and neon gas. The [O III] 5008 Å line emission and the NIRCam images show a complex kinematical and morphological structure where two bright main and three faint clumps are identified in a 10 kpc extent. The system is not classified as a purely rotation-dominated disk. The multiple clumps are instead consistent with a merger-related origin, including either distinct galaxies in interaction or star-forming clumps formed through tidal gas compression during a merger. The spatially resolved emission line fluxes show that dust attenuation, metal enrichment, and ionization parameter are preferentially enhanced in the star formation peaks. Our spectral energy distribution fitting suggests that the main clumps are in a moderately dust-attenuated star-forming phase ($A_V = 0.2$–0.3 and SFR(Hα) $\sim 10\,M_\odot\,\mathrm{yr}^{-1}$) with almost zero escape fraction of ionizing photons. In contrast, the subclumps are dust-free and lying on or below the main sequence of star-forming galaxies. These subclumps may work as a perturber that triggers the clumpy starburst in the surrounding gas through the merger event.

Unified Astronomy Thesaurus concepts: Galaxy mergers (608); Galaxy formation (595); Galaxy evolution (594); High-redshift galaxies (734); James Webb Space Telescope (2291)

1. Introduction

Understanding how galaxies form and evolve requires spatially and kinematically resolved views of their internal structure. Integral field spectroscopy (IFS) is a powerful technique for probing internal structures such as star-forming regions and the interstellar medium (ISM). Ground-based IFS instruments, assisted by adaptive optics (AO), revealed the morphological and kinematic evolution of galaxies up to redshift $z \sim 2$–3 (e.g., R. Genzel et al. 2006, 2008; N. M. Förster Schreiber et al. 2009; D. R. Law et al. 2009; A. Gnerucci et al. 2011; T. Contini et al. 2012; E. Wisnioski et al. 2015; J. P. Stott et al. 2016; N. M. Förster Schreiber et al. 2018). With the advent of the James Webb Space Telescope (JWST; J. P. Gardner et al. 2023) and the Atacama Large Millimeter/submillimeter Array (ALMA; A. Wootten & A. R. Thompson 2009), it has become possible to study galaxies at $z \gtrsim 6$ with unprecedented spatial and spectral resolution, enabling rapid progress in characterizing star formation, feedback, and chemical enrichment processes in the reionization era (e.g., R. Smit et al. 2018; Y. Fudamoto et al. 2022; E. Parlanti et al. 2023; S. Arribas et al. 2024; C. Giménez-Arteaga et al. 2024; G. C. Jones et al. 2024b, 2025; C. Marconcini et al. 2024; Y. Xu et al. 2024; K. Telikova et al. 2025).

Previous studies have shown that galaxies at high redshift exhibit irregular morphologies and disturbed kinematics, such as clumpy structures and asymmetric velocity fields (e.g., Y. Guo et al. 2015; E. Wisnioski et al. 2015; T. Shibuya et al. 2016, 2025; R. C. Simons et al. 2016; M. Rodrigues et al. 2017; Z. Chen et al. 2023; Y. Harikane et al. 2025; J. Scholtz et al. 2025; Y. Sugahara et al. 2025). The increasing prevalence of such irregular systems toward earlier cosmic times is broadly consistent with the rising galaxy major merger rate, which is predicted to scale as $\propto (1+z)^{2-3}$ (e.g., O. Fakhouri & C.-P. Ma 2008; C. J. Conselice et al. 2009; V. Rodriguez-Gomez et al. 2015; Q. Duan et al. 2025). Mergers are known to disrupt both morphology and kinematics, often enhancing gas accretion and triggering bursts of star formation (J. C. Mihos & L. Hernquist 1994, 1996; J. E. Barnes & L. Hernquist 1996; P. Di Matteo et al. 2007; but see also J. Fensch et al. 2017). Recent JWST observations have further revealed extreme examples of merger-driven systems at high redshift, including multi-galaxy assemblies with numerous clumps and extended ionized gas structures (e.g., W. Hu et al. 2025). Beyond mergers, theoretical studies have shown that gas-rich and highly turbulent disks at high redshift are inherently susceptible to gravitational instability, which can give rise to massive star-forming clumps (e.g., M. Krumholz & A. Burkert 2010; A. B. Romeo et al. 2010; J. C. Forbes et al. 2014; A. B. Romeo & O. Agertz 2014; S. Inoue et al. 2016). Simulations also have suggested that cold gas inflows along cosmic filaments, referred to as "cold streams," can drive violent disk instabilities, leading to the formation of massive star-forming clumps within gas-rich disks (e.g., A. Dekel et al. 2009; D. Ceverino et al. 2010; A. Dekel & M. R. Krumholz 2013; N. Mandelker et al. 2017). These scenarios provide theoretical support for the prevalence of clumpy galaxies at high redshift.

At the same time, recent ALMA and JWST observations have revealed massive, rotation-dominated disk galaxies even at $z > 3$, with dynamical properties comparable to those of nearby spiral galaxies (M. Neeleman et al. 2020; F. Rizzo et al. 2020; T. Tsukui & S. Iguchi 2021; L. Costantin et al. 2023; H. Umehata et al. 2025; see also E. Parlanti et al. 2023, 2024; S. Fujimoto et al. 2025). This growing diversity of morpho-kinematic structures in the early Universe underscores the need for spatially and spectrally resolved studies of galaxies at $z > 6$. Such observations are essential for understanding the physical mechanisms that regulate star formation modes and for revealing the role of galaxies in the cosmic reionization.

This study is part of the RIOJA project: "the Reionization and the ISM/Stellar Origins with JWST and ALMA" (JWST GO1 PID1840; PIs: J. Álvarez-Márquez and T. Hashimoto; J. Álvarez-Márquez et al. 2021; T. Hashimoto et al. 2023a; Y. Sugahara et al. 2025; Y. W. Ren et al. 2025). The project aims to investigate galaxy evolution during the cosmic reionization through joint analyses of high-resolution IFS and imaging data. A key feature of RIOJA is the use of ALMA-detected [O III] 88 μm emitters as anchor targets, which enables detailed, multiphase ISM studies when combined with JWST/NIRSpec IFS and NIRCam imaging data.

One of the RIOJA program targets, COS-2987030247 (hereafter COS-2987), located at (R.A., decl.) = $(10^{\mathrm{h}}00^{\mathrm{m}}29\overset{\mathrm{s}}{.}87, +2^\circ13'02\overset{\prime\prime}{.}47)$, has been the subject of intensive study since the pre-JWST era. This galaxy was initially identified by R. Smit et al. (2015) as a $z \sim 6.8$ Lyman break galaxy with an extreme Spitzer/IRAC (G. G. Fazio et al. 2004) $[3.6] - [4.5]$ color, indicative of strong [O III] 5008 Å + 4960 Å+Hβ emission. Its well-constrained photometric redshift and large [O III] 5008 Å equivalent width (EW) made it an excellent candidate for follow-up studies with ALMA. R. Smit et al. (2018) subsequently detected luminous [C II] 158 μm emission from COS-2987 and identified a clear velocity gradient, suggesting a possible rotating disk. N. Laporte et al. (2017) conducted deep near-infrared spectroscopy and detected Lyα emission, suggesting the presence of an early ionized bubble surrounding the galaxy. More recently, J. Witstok et al. (2022) and A. C. Posses et al. (2023) presented spatially resolved ALMA observations of [O III] 88 μm and [C II] 158 μm. J. Witstok et al. (2022) found that the [O III] 88 μm emission is compact and aligns with the UV morphology, whereas [C II] 158 μm appears more extended, reflecting a multiphase ISM and possibly enhanced α-element abundances. A. C. Posses et al. (2023) modeled the [C II] 158 μm kinematics using $^{\mathrm{3D}}$`BAROLO` (E. M. Di Teodoro & F. Fraternali 2015) and found that COS-2987 is consistent with a rotating, low-dispersion disk viewed nearly face-on, although the presence of faint extended structures leaves open the possibility of a compact merger. These pre-JWST studies established COS-2987 as a benchmark system for probing the ISM and dynamical conditions in the epoch of reionization.

With the advent of JWST, whose unprecedented sensitivity and spatial resolution enables detailed mapping of the rest-frame optical emission at high redshift, the disk-like interpretation of COS-2987 has begun to shift. High-resolution NIRCam imaging reveals that COS-2987 is not a smooth, monolithic structure, but instead comprises multiple clumps, suggesting a more complex dynamical state. Y. Harikane et al. (2025) analyzed a large sample of spectroscopically confirmed galaxies at $z = 7$–14, including COS-2987, and found that $\sim$70 % of UV-luminous galaxies at $z \sim 7$ exhibit clumpy morphologies indicative of merger-induced starburst activity. Y. Harikane et al. (2025) performed spectral energy distribution (SED) fitting for individual clumps in COS-2987, but their analysis is based solely on imaging data. In contrast, our study combines JWST/NIRCam imaging with JWST/NIRSpec IFS and ALMA spectroscopy, offering spatially resolved line diagnostics as well as comprehensive SED fitting. This approach allows for a more accurate derivation of key physical quantities for each clump, and more importantly, facilitates the construction of a coherent physical picture of the galaxy at reionization era.

This paper is organized as follows. Section 2 describes the JWST and ALMA observations and data reduction. Section 3 presents spatially resolved emission-line analyses based on [O III] 5008 Å, including kinematic and morphological properties. Section 4 focuses on SED analyses of individual clumps using multiwavelength photometry and spectroscopy. In Section 5, we combine all of the observational results and physical diagnostics to construct a comprehensive physical picture of COS-2987, offering an integrated interpretation of

Table 1
Summary of NIRCam Observations

Filter	Program ID[a]	Exposure Time (hr)	PSF FWHM (arcseconds)	Depth in 2 × PSF FWHM[b] (nJy)	Depth in 0.″5[b] (nJy)
F115W	1837, 1840	0.92	0.06	7.0	48.0
F150W	1837, 1840	0.85	0.06	6.7	40.3
F200W	1837, 1840	0.90	0.07	6.0	34.0
F250M	1840	0.23	0.12	62.2	169.7
F277W	1837	0.70	0.12	8.8	22.3
F335M	1840	0.20	0.14	44.5	92.2
F356W	1837	0.70	0.14	9.8	19.7
F444W	1837, 1840	0.85	0.16	15.2	27.7

Notes.
[a] JWST program ID. No. 1837: PRIMER (J. S. Dunlop et al. 2021); No. 1840: RIOJA (J. Álvarez-Márquez et al. 2021).
[b] The 5σ limiting flux with 2 × point-spread function (PSF) FWHM and 0.″5 diameter apertures were estimated from random aperture photometry on blank sky region.

its internal structure, evolutionary state, and the possible physical origin of its clumpy morphology. This section also serves as the conclusion of the paper. Throughout this paper, we adopt a cosmology with $H_0 = 70\,\mathrm{km\,s^{-1}\,Mpc^{-1}}$, $\Omega_M = 0.3$, and $\Omega_\Lambda = 0.7$. We assumed a Chabrier initial mass function (IMF; G. Chabrier 2003).

2. Observation and Calibration

2.1. JWST NIRCam

The JWST data were obtained as part of the RIOJA project. The specific observations can be accessed via the Mikulski Archive for Space Telescopes (MAST) at the Space Telescope Science Institute: doi:10.17909/c5cd-b767.

We used NIRCam data taken in the two JWST GO1 program Nos. 1840 (RIOJA) and 1837 (PRIMER; PI: J. Dunlop; J. S. Dunlop et al. 2021). In total, six broad bands and two medium bands of data are used in this work. The observational details are summarized in Table 1. All raw data were reduced using the JWST pipeline version 1.17.1 (H. Bushouse et al. 2022) under CRDS context `jwst_1321.pmap`. We also applied custom procedures that are the same as those in T. Hashimoto et al. (2023a) and Y. Sugahara et al. (2025): (1) snowball and wisps correction as described in M. B. Bagley et al. (2023), and (2) a background homogenization before stacking all exposures following P. G. Pérez-González et al. (2023). For further improving the overall background characterization, we applied `NoiseChisel` (M. Akhlaghi & T. Ichikawa 2015; G. Golini et al. 2024), which creates suitable masks of every source covering diffuse emission from galaxy outskirts and bright star spikes (P. G. Pérez-González et al. 2025). The final mosaics are all drizzled with a pixel scale of 0.″03 pix^{-1}.

The point-spread function (PSFs) were derived by stacking $N = 20$–70 point sources in each band image. The corresponding FWHMs range from 0.″06 to 0.″16 (Table 1). We cutout ∼20″ × 40″ regions of uniform depths around COS-2987 for the derivation of the limiting flux. We measured noise fluctuation by $N = 500$ random aperture photometry on blank sky region. To match aperture sizes used for actual photometry to multiple clumps in COS-2987 (Section 4.1), we repeated the random aperture photometry changing the aperture diameter from 0.″1 to 2.″0. The 5σ limiting fluxes in the cases with aperture diameters = 0.″5 and 2× PSF FWHM are shown in Table 1.

We calibrated the astrometry of the NIRCam images using the GAIA DR3 stars (Gaia Collaboration et al. 2016). We carefully selected $N = 4$–15 GAIA stars that are not saturated in the NIRCam images. After the absolute calibration using the GAIA stars, we further corrected for relative positional offset among the filters, where the point sources in F444W were used as the World Coordinate System (WCS) reference. The WCS solutions were estimated using `IRAF` (D. Tody 1986, 1993). We eventually achieved astrometric accuracy of $\lesssim$0.″02 against both the GAIA stars and the F444W reference objects.

2.2. JWST NIRSpec IFS

As part of the RIOJA project, we conducted NIRSpec IFS observations of COS-2987 on 2023 May 26. The observations were taken with a grating/filter pair of G395H/F290LP that produced a cube with a spectral resolution of $R \sim 2700$ in a wavelength range of 2.87–5.27 μm. Four dithers were set with a medium size cycling dither pattern. The total on-source integration time was 2626 s.

We reduced the raw data with the JWST pipeline version 1.14.0 under CRDS context `jwst_1223.pmap`. Following the data reduction process used by GTO programs (e.g., M. A. Marshall et al. 2023; M. Perna et al. 2023; H. Übler et al. 2023) and our previous RIOJA work (T. Hashimoto et al. 2023a), we applied some modifications to the pipeline including (1) the removal of the $1/f$ noise (e.g., M. B. Bagley et al. 2023), (2) rejection of the bad pixels and cosmic rays by sigma-clipping, and (3) removal of a median background in the calibrated images. The data cube was sampled with a pixel size of 0.″05. A scale of the pixel along the spectral direction (spectral element) is 6.65 Å corresponding to 40–70 km s^{-1}, which is high enough to sample the spectral resolution of 80–150 km s^{-1}. The effective area is about 3.″8 × 3.″8.

To set the accurate astrometry, we cross-correlated the NIRSpec [O III] 5008 Å integrated intensity map with the NIRCam F356W image using peak positions of three significantly detected objects (mN, mS, and sN1 in Section 4.1). The reference NIRCam F356W image is significantly contaminated by the [O III] 5008 Å emission by ∼32%. The astrometric accuracy is <0.″01 against the F356W image.

We also used NIRSpec IFS data of the A3V standard star "1808347" (2MASS J18083474+6927286) to evaluate the PSF at each spectral element in the 3D cube. The data were taken in the commissioning program (PID1128; PI: N. Lützgendorf) with the same filter and grating as ours. We reduced the standard star data with the same JWST pipeline version and CRDS context as for COS-2987.

2.3. ALMA

Archival ALMA data in Bands 5 (V. Belitsky et al. 2018), 6 (G. A. Ediss et al. 2004), and 8 (Y. Sekimoto et al. 2008) are available for COS-2987. These data were taken aiming at detection of the [N II] 205 μm, [C II] 158 μm, and [O III] 88 μm lines and dust continuum.

We re-analyzed the Band 8 data because we compare morphology and line profile between ALMA [O III] 88 μm and NIRSpec [O III] 5008 Å in a companion paper (M. Usui et al. 2025). The raw data are the same as in J. Witstok et al. (2022), obtained in ALMA Cycle 6 program (PID: 2018.1.00429.S; PI: R. Smit). The data reduction was performed with the Common Astronomy Software Application (`CASA`; J. P. McMullin et al. 2007; CASA Team et al. 2022) version 5.6. We produced line cube and continuum image using the `tclean` task with the natural weighting to maximize sensitivity for point sources. No *uv*-tapering was adopted. In the line cube construction, we set the channel width as 30 km s^{-1}. The [O III] 88 μm line emission is clearly detected, whose redshift and morophology are consistent with those of J. Witstok et al. (2022). Typical noise rms around the [O III] 88 μm line is 0.576 mJy per 30 km s^{-1} bin. We integrated the cube data over a velocity range of 480 km s^{-1} centered at the [O III] 88 μm line peak. In this [O III] 88 μm line integrated intensity map, the beam size is $0\farcs80 \times 0\farcs61$ with a position angle of 86°, and the noise rms is 82.6 mJy beam^{-1} km s^{-1}. In the continuum image construction, we excluded the spectral window that includes the redshifted [O III] 88 μm line. The beam size of the continuum map is $0\farcs82 \times 0\farcs62$ with a position angle of 86°, and the noise rms is 70.4 μJy beam^{-1}. COS-2987 is not detected in this continuum image, consistent with J. Witstok et al. (2022).

In Band 5, we used measurements of J. Witstok et al. (2022). They reduced the data taken in ALMA Cycle 6 program (PID: 2018.1.01551.S; PI: R. Smit), resulting in the beam size of $0\farcs8 \times 0\farcs7$ and the noise rms of 0.166 mJy beam^{-1} per 48 km s^{-1} bin. They produced the continuum image by averaging over all available spectral channels with natural weighting. The noise rms in the continuum image is 6.47 μJy beam^{-1}. They detect neither [N II] 205 μm emission line nor dust continuum for COS-2987.

In Band 6, we used measurements of A. C. Posses et al. (2023) who combined data taken in two ALMA programs (PID: 2015.1.01111.S; PI: R. Smit and PID: 2018.1.01359.S; PI: M. Aravena). They achieved high angular resolution, beam size $= 0\farcs44 \times 0\farcs35$. The noise rms is 0.134 mJy beam^{-1} per 30 km s^{-1} bin and 6 μJy beam^{-1} for the line cube and continuum image, respectively. They detected the [C II] 158 μm line emission from COS-2987 that is spatially resolved thanks to the high angular resolution. On the other hand, dust continuum is not detected.

3. Emission-line Analyses in the NIRSpec IFS Data

3.1. Emission-line Search

In the reduced NIRSpec IFS data cube, we identified bright [O III] 5008 Å line emission at $z \approx 6.81$. To accurately determine the redshift and search for other emission lines, we extracted 1D spectrum using `photutils` (L. Bradley et al. 2023) with an elliptical aperture whose center position, semimajor axis, semiminor axis, and position angle are (R.A., decl.) $= (10^{\rm h}00^{\rm m}29\fs870, +2°13'02\farcs266)$, $0\farcs45$, $0\farcs30$, and $27\fdg2$, respectively. This aperture roughly covers the two brightest emission peaks (mN and mS in Section 3.2). We set this relatively small aperture to optimize signal-to-noise ratio (SNR) and used it only for the emission-line search. The aperture and extracted 1D spectrum are shown in Figure 1. We estimated the associated error spectrum by measuring standard deviation of the flux density over a wavelength range within ± 0.05 μm centered on each spectral element.

We searched for the following emission lines[21]: [O II] 3727,3730 Å doublet, H9, [Ne III] 3870 Å, H8, He I 3966 Å, Hϵ, He I 4027 Å, Hδ, Hγ, [O III] 4364 Å, He I 4473 Å, He II 4687 Å, Hβ, He I 4923 Å, [O III] 4960 Å, [O III] 5008 Å, He I 5017 Å, He I 5877 Å, [N II] 6550 Å, Hα, [N II] 6585 Å, He I 6680 Å, [S II] 6718 Å, and [S II] 6733 Å. Gaussian profile fits were applied to the spectra cutout around expected wavelengths of the above lines at $z \approx 6.81$. Since the purpose of this fitting is to evaluate the significance of the line detection, we avoid fixing the redshift and line width to those of the brightest [O III] 5008 Å. For the [O II] 3727,3730 Å doublet, we fit the cutout spectrum with double Gaussian profiles whose separation was fixed and widths were set to be the same. The best-fit Gaussian profiles to the bright lines are shown in Figure 1. The horizontal axis is the velocity relative to the best-fit redshift to [O III] 5008 Å, $z = 6.80731 \pm 0.00002$. To evaluate the fitting uncertainty, we followed a Monte Carlo (MC) manner. We repeatedly performed the Gaussian profile fitting to 1000 mock spectra that were generated by perturbing the observed spectrum. Fluctuation of the best-fit parameters from the 1000 iterations defines 68% confidential intervals (1σ errors) of the line properties such as redshift, flux, and line width.

We calculated two types of SNRs for each line: peak flux density SNR and integrated flux SNR. We also produced line intensity maps for visual inspection by integrating the data cube over a wavelength range corresponding to 3× FWHM around the line peak. We set detection criteria as follows: (1) peak SNR $\geqslant 2$, (2) integrated SNR $\geqslant 3$, and (3) good in visual inspection of the integrated intensity map as well as the cube data. If a given line passes all or two of the three criteria, the line is regarded as detection. Otherwise, we consider the line as nondetection. While only the second criterion on the integrated SNR may be enough as shown in some previous works using JWST NIRSpec MSA data (e.g., I. H. Laseter et al. 2024; T. Morishita et al. 2024b), the IFS data allow us to more robustly determine whether a given line is detected by the third criterion. In COS-2987, the detected lines are [O II] 3727,3730 Å doublet, [Ne III] 3870 Å, Hγ, [O III] 4364 Å, Hβ, [O III] 4960 Å, [O III] 5008 Å, and Hα. While the [O III] 4364 Å line appears faint in the integrated intensity map, its

---

[21] The rest-frame wavelengths of the emission lines are extracted from Linetools (J. X. Prochaska et al. 2017) and Atomic Spectra Database (A. Kramida et al. 2020) in vacuum.

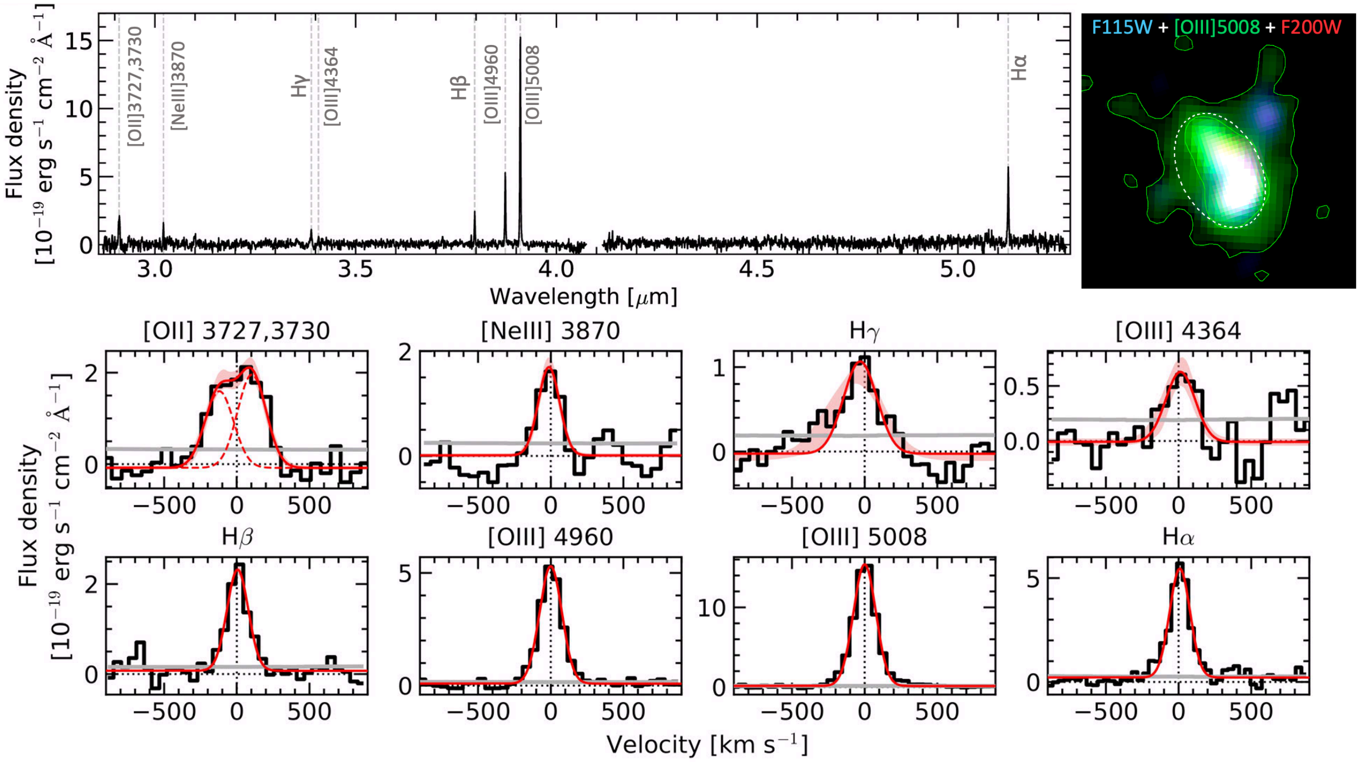

Figure 1. Top-left panel: 1D spectrum of COS-2987 extracted from the NIRSpec IFS data cube. Vertical dashed lines indicate the detected emission lines. Top-right panel: the aperture used for extraction of the spectrum is shown by a dashed ellipse, which is superposed on the F115W (blue) + [O III] 5008 Å (green) + F200W (red) pseudo-color image. These three images were smoothed so that their PSFs are matched (Section 4.1). Contours show the [O III] 5008 Å integrated intensity map at 2× and 10 × σ. Panel size is 2″ × 2″ corresponding to 11.6 kpc × 11.6 kpc at $z = 6.81$. Bottom panels: zoomed-in spectra of the detected emission lines, where the horizontal axis is the velocity relative to the best-fit redshift to [O III] 5008 Å, $z = 6.80731$. In each panel, the black solid histogram and gray line indicate the observed and 1σ error spectra, respectively. The red solid line and red shade show the best-fit Gaussian profile and 68% confidential interval from the MC iteration (see the text). For the [O II] 3727,3730 Å doublet, the best-fit models for individual lines are shown by the red dashed lines.

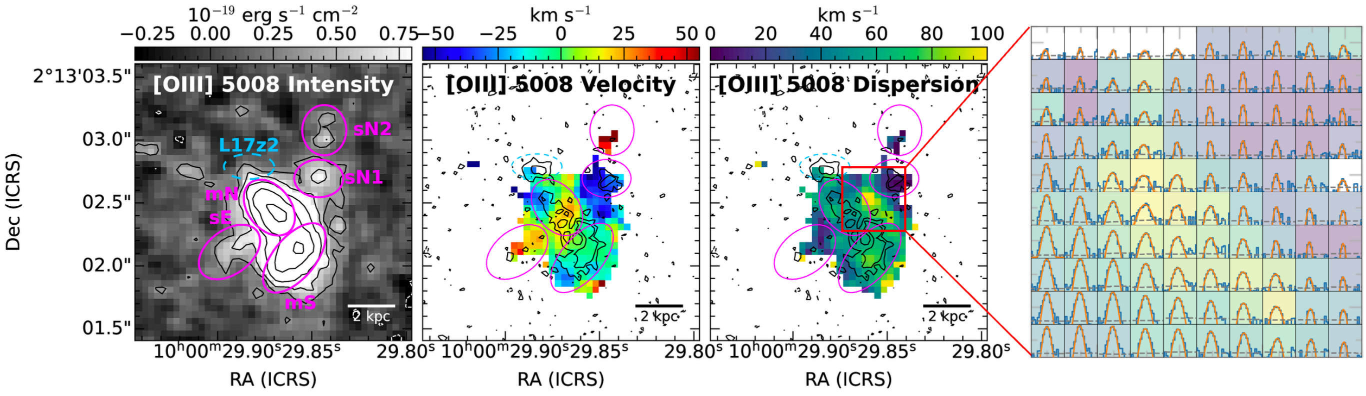

Figure 2. The [O III] 5008 Å line integrated intensity (left panel), velocity (middle panels), and velocity dispersion (right panel) maps. Each panel has 2″2 × 2″2 in size. Ellipses correspond to the photometric apertures for the multiple clumps (Section 4.1). Contours in the integrated intensity map are −2 (dashed), 2, 4, 8, 16, and 32 × σ (solid) of the line brightness. Contours in the velocity and velocity dispersion maps show the F115W surface brightness profile before the PSF-matching at −2 (dashed), 2, and 4 × σ (solid) levels. The F115W surface brightness is sensitive to 100 Myr timescale star formation. The rightmost panel is also the velocity dispersion map but zoomed in around the highest velocity dispersion region between mN and sN1. We also superposed the observed (blue), error (gray dashed) spectra, and the best-fit Gaussian profile (orange) on each pixel.

peak and integrated SNRs are as high as 3.3 and 4.2, respectively. These SNR levels are usually considered detection (K. Nakajima et al. 2023; I. H. Laseter et al. 2024; T. Morishita et al. 2024b).

3.2. Morphology and Kinematics in [O III] 5008 Å

We investigated the morphology and kinematics of COS-2987 using [O III] 5008 Å that has the highest SNR among the lines. Figure 2 shows the integrated intensity, velocity, and velocity dispersion maps of [O III] 5008 Å. The line intensity map was produced following the same procedure described in Section 3.1. To produce the velocity and velocity dispersion maps, we performed a Gaussian profile fit for the spectrum at each spatial pixel in the cube data (commonly used technique; e.g., R. Smit et al. 2018; H. Übler et al. 2019; T. Tokuoka et al. 2022; M. Perna et al. 2023). The fitting procedures are the same as those adopted for the integrated spectrum

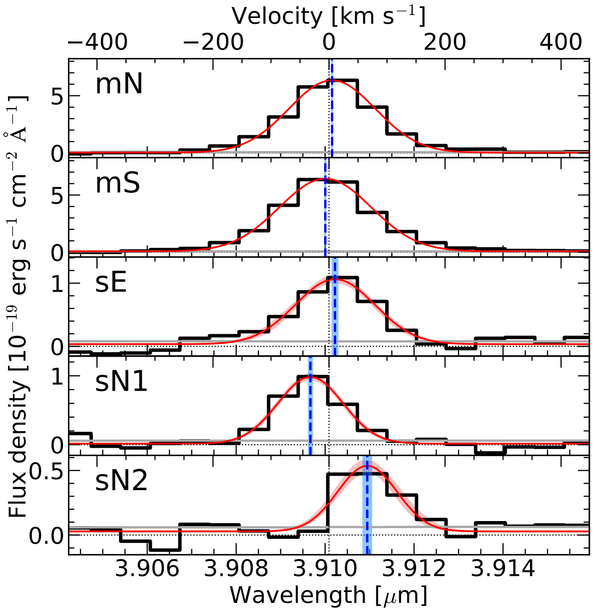

Figure 3. The [O III] 5008 Å line profiles of the five clumps. The velocity axis is centered at $z = 6.80731$. In each panel, the black solid histogram and gray line indicate the observed and 1σ error spectra, respectively. The red solid line and red shade show the best-fit Gaussian profile and 68% confidential interval from the MC iteration. The blue vertical dashed line and shade indicate the best-fit peak velocity and uncertainty of each clump.

(Section 3.1). The velocity dispersion was corrected for the instrumental spectral resolution (P. Jakobsen et al. 2022). We masked spatial pixels where the fitting significance was $<5\sigma$. The fitting significance was evaluated from the χ^2 distribution (T. Tokuoka et al. 2022).

The line integrated intensity map (the left panel in Figure 2) shows a complex morphology. On this map, we visually identified five spatially distinct structures showing either a clear local intensity peak or a linear, tail-like extension. The [O III] 5008 Å flux of COS-2987 mainly comes from two main north and south peaks, which we refer to as "mN" and "mS" clumps. In the northwest direction from these central clumps, there are two other fainter peaks. We refer to these substructures as "sN1" and "sN2" clumps. We identified a tail-like substructure "sE" extending southeast of the mN clump. Throughout this paper, we use the term "clump" in an observational sense to refer to spatially distinct regions identified in the NIRSpec IFS and NIRCam data.[22]

In the velocity map (middle panel in Figure 2), the five clumps have different velocities. We quantitatively evaluated the velocity differences by the clumps (Section 4.1) and along a given axis (Appendix A). Figure 3 shows [O III] 5008 Å line profiles of the five clumps, where the peak velocities and uncertainties relative to $z = 6.80731$ are shown by vertical dashed lines and shades. These velocity offsets are also shown in Table 2. Compared to mN, sN1 is blueshifted by -37 km s^{-1}, and sN2 is redshifted by $+61$ km s^{-1}. The positive velocity of sE relative to mN, $\Delta v = 5$ km s^{-1}, is not significant due to the large uncertainty of the faint sE tail. The velocity difference between mN and mS, ∼12 km s^{-1}, is significant beyond the uncertainty. While this velocity difference is smaller than the spectral element scale by a factor of ∼5, such a subpixel scale difference is commonly reliable for the high-SNR lines (e.g., R. Teague & D. Foreman-Mackey 2018). In mN, further resolved motion can be seen: redshifted (blueshifted) in the southwest (northeast) part. This may suggest a rotation or smaller size substructures in mN.

In the right panel of Figure 2, there is a velocity dispersion peak at the boundary of mN and sN1. In the velocity and velocity dispersion maps of Figure 2, NIRCam F115W surface brightness is superposed by the contours. The F115W band samples the rest-frame 1500 Å light and is sensitive to the 100 Myr scale star formation. The velocity dispersion peak between mN and sN1 is interesting where no corresponding star formation nor line flux peak is observed (Section 4.1).

We now investigate whether the kinematics of COS-2987 are consistent with a merger or a rotation disk. We measured an observed velocity difference ($\Delta v_{\rm obs}$) and intrinsic velocity dispersion (σ_0) following an approach applied to IFS data from the KMOS$^{\rm 3D}$ survey of $0.7 \lesssim z \lesssim 2.7$ galaxies (E. Wisnioski et al. 2015; P. Lang et al. 2017; N. M. Förster Schreiber et al. 2019; E. Wisnioski et al. 2019). The $\Delta v_{\rm obs}$ corresponds to the rotation velocity if the system is an edge-on rotating disk. The σ_0 is a representative velocity dispersion per pixel taking account of the beam smearing effect (N. M. Förster Schreiber et al. 2009, 2014; S. F. Newman et al. 2013), which is practically measured at the galaxy outskirt and gets smaller than a simple average of the velocity dispersion map. Details are described in Appendix A. The measured $\Delta v_{\rm obs}$ and σ_0 are 34 km s^{-1} and ∼30 km s^{-1}, respectively.

We applied criteria to judge a rotating disk proposed by E. Wisnioski et al. (2015): (1) the given galaxy exhibits a continuous velocity gradient along a single axis, (2) rotationally supported $v_{\rm rot}/\sigma_0 > 1$, (3) the position of the steepest velocity gradient is coincident with the velocity dispersion peak, (4) the photometric and kinematic major axes are in agreement, and (5) the position of the steepest velocity gradient is coincident with the centroid of the continuum. The rotation velocity is expressed as $v_{\rm rot} = \Delta v_{\rm obs}/\sin(i)$, where i is an inclination of the galaxy. The measured $v_{\rm rot}/\sigma_0 = 1.1/\sin(i)$ satisfies the second criterion, regardless of the inclination i. The position of the steepest velocity gradient is the midpoint between mN and sN1 (the kinematic center defined in Appendix A). The kinematic major axis is defined as the direction of the largest observed velocity difference that passes through sE, mN, and sN1 (Appendix A). The photometric axis (the stellar axis in Appendix A) aligns the F115W surface brightness or stellar distribution penetrating the two continuum centroids at mN and mS. COS-2987 satisfies only criteria (2) and (3). We note that the frequently used second criterion involves uncertainties in not only the measurements but also the threshold. COS-2987 does not satisfy the modified version of the second criterion, $v_{\rm rot}/\sigma_0 > \sqrt{3.36}$ (N. M. Förster Schreiber et al. 2018; E. Wisnioski et al. 2019), if the inclination $i > 37°$. Also, some authors use $\Delta v_{\rm obs}/\sigma_{\rm tot} > 0.4$ with $\sigma_{\rm tot}$ measured from spatially integrated spectrum (e.g., R. Smit et al. 2018; T. Tokuoka et al. 2022). Combining the multiple criteria is essentially important for robust kinematic classification, which is made possible by high-resolution IFS instruments such as JWST NIRSpec.

In our NIRSpec IFS data, COS-2987 is not classified as a purely rotation-dominated disk. The multiple clumps in the [O III] 5008 Å emission can be interpreted as merger-related

---

[22] The term "clump" in this paper does not necessarily correspond to a stellar system typically assumed to form within a host galaxy.

Table 2
Observed Measurements in NIRSpec IFU, NIRCam, and ALMA Data

	mN	mS	sE	sN1	sN2	Total
Redshift[a]	6.80745 ± 0.00002	6.80714 ± 0.00002	6.80758 ± 0.00013	6.80648 ± 0.00009	6.80903 ± 0.00019	6.80726 ± 0.00002
Velocity[b] (km s^{-1})	5.3 ± 0.7	−6.4 ± 0.8	10.3 ± 4.9	−32.1 ± 3.4	66.0 ± 7.4	−2.1 ± 0.9
FWHM[c] (km s^{-1})	134.8 ± 2.0	149.0 ± 2.2	116.4 ± 13.8	70.3 ± 8.0	43.9 ± 10.8	144.0 ± 2.6
$F_{\rm [O\,II]3727}$ (10^{-18} erg s^{-1} cm^{-2})	1.33 ± 0.3	1.89 ± 0.25	0.51 ± 0.19	<0.44	<0.3	7.12 ± 0.87
$F_{\rm [O\,II]3730}$ (10^{-18} erg s^{-1} cm^{-2})	1.83 ± 0.31	2.22 ± 0.39	0.63 ± 0.22	<0.46	<0.46	7.6 ± 1.17
$F_{\rm [Ne\,III]3870}$ (10^{-18} erg s^{-1} cm^{-2})	1.22 ± 0.2	1.17 ± 0.18	<0.37	<1.48	<0.53	4.39 ± 0.57
$F_{\rm H\gamma}$ (10^{-18} erg s^{-1} cm^{-2})	1.08 ± 0.49	1.11 ± 0.23	<1.55	<0.37	<0.29	2.53 ± 0.97
$F_{\rm [O\,III]4364}$ (10^{-18} erg s^{-1} cm^{-2})	1.01 ± 0.33	<0.53	<0.32	<0.26	<0.05	1.83 ± 0.5
$F_{\rm H\beta}$ (10^{-18} erg s^{-1} cm^{-2})	2.02 ± 0.2	2.32 ± 0.23	<0.47	0.34 ± 0.39	<0.24	7.98 ± 0.79
$F_{\rm [O\,III]4960}$ (10^{-18} erg s^{-1} cm^{-2})	5.22 ± 0.52	5.36 ± 0.54	0.76 ± 0.11	0.75 ± 0.12	< 0.25	17.4 ± 1.8
$F_{\rm [O\,III]5008}$ (10^{-18} erg s^{-1} cm^{-2})	15.37 ± 1.54	16.46 ± 1.65	2.31 ± 0.23	1.78 ± 0.18	0.85 ± 0.09	52.3 ± 5.43
$F_{\rm H\alpha}$ (10^{-18} erg s^{-1} cm^{-2})	6.19 ± 0.62	6.98 ± 0.7	1.0 ± 0.25	0.82 ± 0.38	<0.53	23.9 ± 2.36
$f_{\nu,\rm F115W}$ (μJy)	0.057 ± 0.005	0.103 ± 0.006	0.021 ± 0.006	0.032 ± 0.004	<0.014	0.351 ± 0.046
$f_{\nu,\rm F150W}$ (μJy)	0.071 ± 0.005	0.12 ± 0.006	<0.017	0.028 ± 0.004	<0.013	0.354 ± 0.046
$f_{\nu,\rm F200W}$ (μJy)	0.077 ± 0.004	0.12 ± 0.006	0.014 ± 0.005	0.028 ± 0.003	<0.011	0.369 ± 0.04
$f_{\nu,\rm F250M}$ (μJy)	0.081 ± 0.021	0.111 ± 0.026	<0.07	<0.049	<0.056	0.458 ± 0.167
$f_{\nu,\rm F277W}$ (μJy)	0.089 ± 0.004	0.131 ± 0.007	0.029 ± 0.003	0.036 ± 0.002	0.01 ± 0.002	0.479 ± 0.025
$f_{\nu,\rm F335M}$ (μJy)	0.103 ± 0.013	0.11 ± 0.016	<0.042	<0.03	<0.034	0.472 ± 0.096
$f_{\nu,\rm F356W}$ (μJy)	0.168 ± 0.008	0.226 ± 0.011	0.043 ± 0.003	0.05 ± 0.003	0.024 ± 0.002	0.836 ± 0.042
$f_{\nu,\rm F444W}$ (μJy)	0.128 ± 0.006	0.175 ± 0.009	0.036 ± 0.004	0.04 ± 0.003	0.014 ± 0.003	0.619 ± 0.031
$F_{\rm [O\,III]88}$ (10^{-18} erg s^{-1} cm^{-2})	…	…	…	…	…	15.37 ± 3.33
$f_{\nu,\rm Band5}$ (μJy)	<22.0	<22.0	<22.0	<22.0	<22.0	<34.5
$f_{\nu,\rm Band6}$ (μJy)	<19.4	<19.4	<19.4	<19.4	<19.4	<48.6
$f_{\nu,\rm Band8}$ (μJy)	<213.1	<213.1	<213.1	<213.1	<213.1	<344.8

Notes. The 3σ upper limits are given for nondetections.

[a] Redshifts estimated by the Gaussian profile fitting to the NIRSpec [O III] 5008 Å line.

[b] Radial velocity offset relative to $z = 6.80731$, which is estimated from the redshifts of the [O III] 5008 Å lines.

[c] Line FWHMs estimated by the Gaussian profile fitting to the NIRSpec [O III] 5008 Å line. They are corrected for the instrumental broadening (P. Jakobsen et al. 2022), the sum of the [O II] 3727Å and [O II] 3730 Å fluxes.

[d] Upper limits on the ALMA continuum flux density are evaluated from the noise rms levels per beam for the individual clumps. For the total photometry, we corrected the noise rms per beam for areal difference between the beam and [O III] 5008 Å emitting region (see the text). The cosmic microwave background (CMB) effects (E. da Cunha et al. 2013; K. Ota et al. 2014) are also corrected.

structures, either merging galaxies or clumps formed through tidal compression during a merger (e.g., Y. Nakazato et al. 2024). Alternatively, they can be star-forming clumps induced by disk instability within a single galaxy. In the latter case, the underlying disk is hard to be observed via the [O III] 5008 Å emission because local star formation in the clumps disturbs warm ionized gas. It is observationally difficult to further distinguish the physical origins of the multiple clumps. We will revisit this issue with simulations and previous ALMA works in Section 5.

3.3. Spatially Resolved Line Diagnostics

The NIRSpec line integrated intensity maps (Section 3.1) are shown in the left panels of Figure 4. To investigate emission-line flux ratios pixel by pixel, we homogenized PSFs of the line integrated intensity maps to that of the NIRSpec Hα integrated intensity map with FWHM = 0.″21 (PSF-matched data; see Appendix B). These PSF-matched line integrated intensity maps are shown in the right panels of Figure 4. From the PSF-matched images, we produced maps of physical quantities: dust attenuation (A_V), 10 Myr timescale star formation rate surface density ($\Sigma_{\rm SFR}$), metallicity ($12 + \log({\rm O/H})$), and ionization parameter ($\log U_{\rm ion}$). We also produced a map of electron density ($\log(n_{\rm e}/{\rm cm}^{-3})$) using the NIRSpec IFU data cube before applying the PSF-matching, based on the [O II] 3729,3730 Å doublet. These maps are shown in Figure 5. In every panel, we superposed the PSF-matched F115W surface brightness in contours that trace the rest-frame 1500 Å continuum and then 100 Myr timescale SFR surface density.

The dust attenuation $A_{\rm V}$ was measured from the Balmer decrement Hα/Hβ assuming the SMC dust extinction law (M. L. Prevot et al. 1984; K. D. Gordon et al. 2003) and the intrinsic line flux ratio of 2.76.[23] We adopted the SMC law, as it is likely applicable to high-z low-mass galaxies (N. A. Reddy

---

[23] The intrinsic Hα/Hβ = 2.76 is the value under assumption of electron temperature of 20,000 K (P. J. Storey & D. G. Hummer 1995; V. Luridiana et al. 2015). This temperature is obtained for COS-2987 in the companion paper (M. Usui et al. 2025).

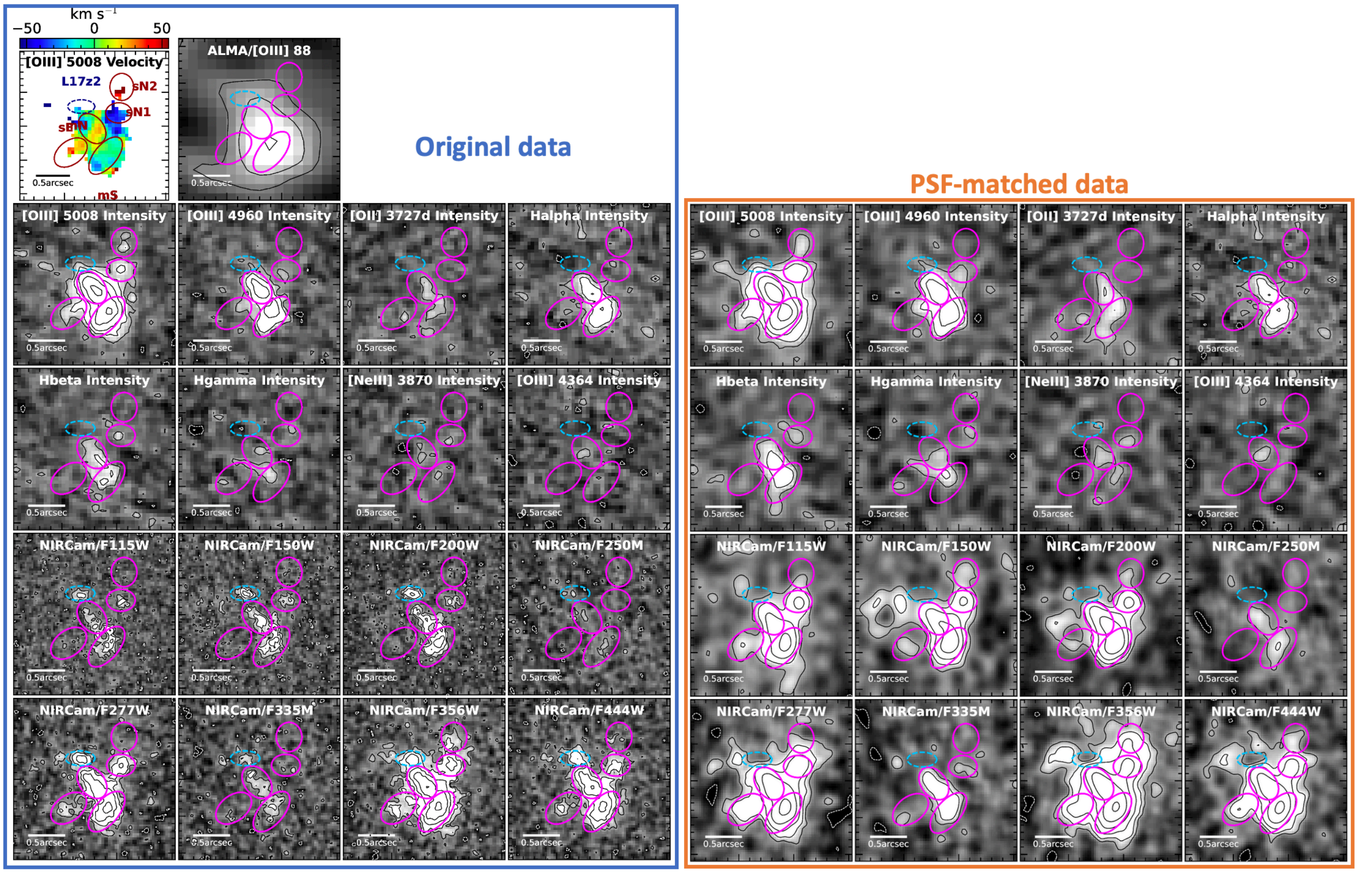

Figure 4. Multiple clumps identified in the NIRSpec line integrated intensity maps and NIRCam images. We also show the [O III] 5008 Å velocity and ALMA [O III] 88 μm integrated intensity maps in the top-left panels. Not only the original data but also the PSF-matched data are shown in the left and right panels, respectively. Each panel has $2''\!.2 \times 2''\!.2$ in size. In all of the panels, the photometric apertures for the multiple clumps are shown by magenta ellipses. Contour levels are -2 (dashed), 2, 4, 8, 16, and $32 \times \sigma$ (solid). The low-z contaminant, L17z2, is masked when generating the PSF-matched NIRCam images (see Section 4.1.1).

et al. 2015; Y. Fudamoto et al. 2017, 2020; but see also N. Scoville et al. 2015; R. J. McLure et al. 2018) and is also supported in the case of COS-2987 (Section 4.2). We masked out pixels with SNR lower than 2 in the Hα or Hβ integrated intensity map. The A_V map in Figure 5 clearly shows spatial variation of the dust attenuation. From comparison with the F115W surface brightness (contours in Figure 5), the dust attenuation is as high as $A_V \sim 1$ mag near the rest-frame UV emission (i.e., young stellar populations) peaks of mN and mS. The A_V peak values are much higher than A_V estimated from the Hα and Hβ fluxes spatially integrated within the clumps: $A_V = 0.28^{+0.38}_{-0.28}$ mag and $0.22^{+0.35}_{-0.22}$ mag for mN and mS, respectively. In the case that dust is distributed inhomogeneously, dust extinction measurements from the spatially integrated Hα/Hβ ratio tend to be biased toward low-extinction regions, underestimating the true amount of dust attenuation (K. Kreckel et al. 2013; E. J. Nelson et al. 2016).

The $\Sigma_{\rm SFR}$ was measured from the Hα flux using a conversion formula used in A. E. Shapley et al. (2023), SFR $= (2.14 \times 10^{42}) \times L({\rm H}\alpha)$, which is tuned for low-metallicity ($Z = 0.27\,Z_\odot$) galaxies under Chabrier IMF. The Hα emission traces 10 Myr timescale star formation. We here corrected for the dust attenuation using the A_V map. The SFR map in Figure 5 shows a similar trend as the A_V map: the $\Sigma_{\rm SFR}$ peaks almost align peaks of young stars (F115W) in mN and mS. The peak and averaged $\Sigma_{\rm SFR}$ are $\sim$9 and $\sim 4\,M_\odot\,{\rm yr}^{-1}\,{\rm kpc}^{-2}$, respectively, both of which are broadly consistent with $\Sigma_{\rm SFR}$ of $5 < z < 14$ galaxies and well above the $z < 3$ measurements (T. Morishita et al. 2024a and references therein).

The metallicity $12 + \log({\rm O/H})$ was estimated from the R3 index following M. Hirschmann et al. (2023), where R3 = [O III] 5008 Å/Hβ. All of the line fluxes were corrected for dust attenuation using the A_V map. The metallicity map of Figure 5 shows variation of $12 + \log({\rm O/H})$ from 7.2–8. These values are comparable to metallicity measurements of $3 < z < 9.1$ galaxies (T. Morishita et al. 2024b). In mN, the metallicity is $12 + \log({\rm O/H}) \sim 7.8$, higher than mS and other regions with $\lesssim$7.6. The metallicity difference between mN and the other regions is significant beyond the uncertainty that was calculated by propagating the line flux errors in each pixel. These internal metallicity variations of $\sim$0.6 dex are similar to those found in other high-z groups of merging galaxies (S. Arribas et al. 2024; G. Venturi et al. 2024). The mN and mS clumps may have originally been distinct galaxies with different evolutionary paths (and then different metal enrichment histories).

The ionization parameter is defined as the ratio of ionizing photon flux to hydrogen atom density (L. J. Kewley & M. A. Dopita 2002) and often expressed as a dimensionless form, $U_{\rm ion}$, by dividing by the speed of light. We used an analytic formulae of K. Nakajima & M. Ouchi (2014) using $12 + \log({\rm O/H})$ and O32 index, where O32 = [O III] 4960,5008 Å/[O II] 3727,3730 Å. All of the line fluxes were corrected for dust attenuation using the A_V map. In the $\log U_{\rm ion}$ map in

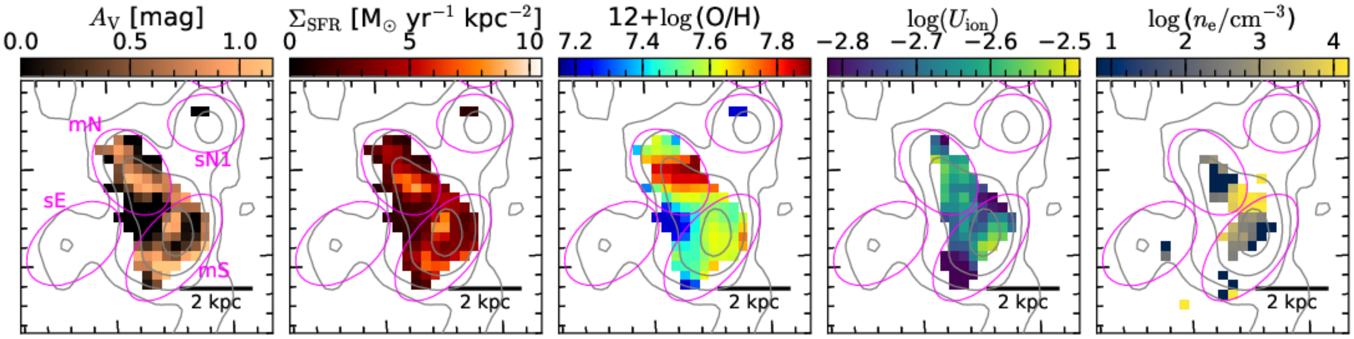

Figure 5. Maps of physical quantities: dust attenuation A_V, 10 Myr timescale (Hα) star formation rate surface density $\Sigma_{\rm SFR}$, metallicity 12 + log(O/H), ionizing parameter log($U_{\rm ion}$), and electron density log(n_e/cm^{-3}) from left to right. Pixel-to-pixel physical properties of A_V, SFR, 12 + log(O/H), log($U_{\rm ion}$), and log(n_e) are derived from Balmer decrement (Hα/Hβ), Hα, R3 index ([O III] 5008 Å, Hβ), O32 index ([O III]5008 Å, [O II] doublet), and [O II] 3727,3730 Å line ratio, respectively. Each panel covers 6.9 × 6.9 kpc at $z = 6.81$. The multiple clumps in COS-2987 are shown by ellipses. Contours show the PSF-matched F115W surface brightness profile at 2, 4, 8, and 16 $\times\sigma$ levels. The F115W surface brightness is sensitive to 100 Myr timescale star formation.

Figure 5, while the map spatial coverage is limited by the [O II] 3727,3730 SNR, we can see spatial variation from $\log U_{\rm ion} = -2.9$ to -2.5. The ionization parameters at any location in COS-2987 are lower than the median value of $z = 7$–9 galaxies in the Cosmic Evolution Early Release Science (CEERS) survey, $\log U_{\rm ion} = -2.1$ (M. Tang et al. 2023), and the typical value of $z = 5.5$–9.5 galaxies in the JADES survey, $\log U_{\rm ion} = -1.5$ (A. J. Cameron et al. 2023)

We derived the map of electron density, log(n_e/cm^{-3}), based on the line ratio of the [O II] 3729,3730 doublet (D. E. Osterbrock & G. J. Ferland 2006). For each spaxel in the NIRSpec IFS cube, we extracted the spectrum around the [O II] doublet and performed a double Gaussian fitting with MC iterations, following the same procedure as in Section 3.1. From the best-fit line fluxes, we calculated the line ratio and converted it to n_e. The resulting electron density map is shown in the rightmost panel of Figure 5. Interestingly, the derived electron densities span more than 3 orders of magnitude, ranging from $n_e \sim 10$ to 10^4 cm^{-3}. This large variation in n_e originates from the measured [O II] line ratios spanning the full theoretical range, from ∼0.3 to ∼1.5 (D. E. Osterbrock & G. J. Ferland 2006). The density variations are significant beyond the uncertainties. Notably, the highest electron densities are found in the region between mN and mS (and possibly sN1), which may suggest that the enhanced densities are related to an ongoing merger between these clumps (e.g., T. J. Cox et al. 2006).

The physical quantities investigated in this section roughly correlate with the spatial distribution of young stars traced by the F115W surface brightness. At the F115W peaks in mN and mS, star formation is more active, dust attenuation is higher, and ionization parameter is higher than at the outskirt regions. The notable exception comes from the metallicity map, where mN has higher values than mS by ∼0.2 dex. Mapping of the physical quantities in subclumps sE, sN1, and sN2 will help the correct understanding, which requires deeper IFS observations in future.

4. Multiwavelength Analysis of the Clumps

4.1. Multiband Photometry

4.1.1. Individual Clumps

Figure 4 shows the NIRCam images and ALMA [O III] 88 μm integrated intensity map as well as the NIRSpec line integrated intensity maps. The five clumps, mN, mS, sE, sN1, and sN2 (magenta ellipses in Figure 4), are well resolved in many bands and line maps except for the ALMA [O III] 88 μm map, which has a coarser spatial resolution. While mN and mS are further divided into smaller structures in the NIRCam F115W image, we investigate the five clumps defined in Section 3.2 in the subsequent multiwavelength analyses.

Before focusing on the five clumps, we mention that there is a $z \sim 2$ interloper (R. Smit et al. 2015; N. Laporte et al. 2017) lying to the northeast of mN (cyan dashed ellipse in Figure 4).[24] We hereafter refer to this object as L17z2. In the following analyses, we masked L17z2 in the NIRCam images. We did not mask it in the NIRSpec data because the low-z interloper should not emit line emission at the specific wavelengths. Actually, L17z2 cannot be seen in the NIRSpec line integrated intensity maps (Figure 4).

For the multiband SED analyses, we used the PSF-matched NIRSpec and NIRCam data (Section 3.2; Appendix B). From the PSF-matched NIRSpec data cube, we extracted 1D spectra of the five clumps whose apertures are defined as the solid ellipses in Figures 2 and 4. In the same manner as in Section 3.1, we measured the [O II] 3727 Å, [O II] 3730 Å, [Ne III] 3870 Å, Hγ, Hβ, [O III] 4960 Å, [O III] 5008 Å, and Hα line fluxes and the uncertainties of the five clumps. We put a lower limit on the flux uncertainty as 10% of the flux to securely take account of the absolute flux uncertainty (T. Böker et al. 2023).[25] We determined detection or nondetection for each line of each clump according to the three criteria introduced in Section 3.1. All of the line fluxes are shown in Table 2. We put 3σ upper limits for nondetections. In Table 2, we also show the redshifts from [O III] 5008 Å and the radial velocity offsets with respect to $z = 6.80731$ that are the fiducial estimate in the central region (Section 3.1).

For the NIRCam flux density of the five clumps, we performed aperture photometry using `photutils`

---

[24] We checked Subaru public optical images from the Subaru strategic program with Hyper Suprime-Cam (HSC-SSP; H. Furusawa et al. 2018; S. Kawanomoto et al. 2018; Y. Komiyama et al. 2018; S. Miyazaki et al. 2018; H. Aihara et al. 2019), and found that L17z2 is detected in the g, r, i, and z bands with significance of 2σ–3σ. This confirms that L17z2 is a lower-z interloper.

[25] See also "JWST Absolute Flux Calibration" in JWST User Documentation: https://jwst-docs.stsci.edu/jwst-calibration-status/jwst-absolute-flux-calibration.

(L. Bradley et al. 2023) on the PSF-matched images (the right panels of Figure 4). We subtracted from the aperture flux local sky background, which was measured using a circular annulus aperture with inner/outer radius of $1''/2''$. The photometric uncertainties were estimated from random aperture photometry described in Section 2.1. In addition, we put a lower limit of 5% on the photometric uncertainty to securely take account of the absolute flux uncertainty (J. Rigby et al. 2023). All bands' flux densities are shown in Table 2. We adopted 3σ upper limits for flux densities below the 3σ detection threshold.

While the [O III] 88 μm line is significantly detected in ALMA Band 8, the relatively coarse resolution does not allow us to spatially resolve mN, mS, sE, sN1, and sN2 clumps (Figure 4). We then measured only the total [O III] 88 μm line flux (Section 4.1.2). Dust continuum emission is not detected in Band 5, 6, nor 8. The sizes of the five clumps are smaller than the beam sizes of the ALMA data. Then, we set three times the noise rms per beam in the ALMA continuum images (Section 2.3) for the flux density upper limit of each clump. We further applied the correction for cosmic microwave background (CMB) effect (E. da Cunha et al. 2013; K. Ota et al. 2014) assuming dust temperature $T_{\rm d} = 50$ K and emissivity index $\beta_{\rm d} = 2.0$ (e.g., L. Sommovigo et al. 2022a, 2022b). The CMB correction factors are 1.13, 1.08, and 1.01 in Bands 5, 6, and 8, respectively. All of the ALMA continuum flux densities are summarized in Table 2.

4.1.2. Total Photometry

To obtain total NIRSpec line fluxes of COS-2987, we extract a spectrum from the PSF-matched data cube with a 2σ isophotal aperture in the [O III] 5008 Å integrated intensity map (the outermost contour in the PSF-matched [O III] 5008 Å panel of Figure 4). Then, we measured the emission-line fluxes in the same manner as in Section 3.1. Although the isophotal aperture is expected to maximize the SNR for total flux (e.g., B. Welch et al. 2024), there may still be flux loss outside the aperture. We performed the curve-of-growth analysis (e.g., A. B. Drake et al. 2017) for the [O III] 5008 Å flux, and found a 10% loss in the 2σ isophotal flux. We applied the aperture correction to the 2σ isophotal fluxes of the all lines assuming the same spatial distribution of ionized gas emitting the nebular lines. The resultant total line fluxes are shown in Table 2.

Because continuum morphology traced by the NIRCam bands is not necessarily similar to the nebular gas morphology, we estimated the total flux densities from convergence values of the curves of growth in the every individual NIRCam bands. They are shown in Table 2. Our NIRCam flux densities are consistent within the uncertainties with previous measurements using the Hubble Space Telescope and ground-based instruments (R. Smit et al. 2015; N. Laporte et al. 2017; H. Nayyeri et al. 2017; J. R. Weaver et al. 2022) as well as the recent work using the PRIMER NIRCam data (Y. Harikane et al. 2025).

In ALMA data, we measured the total [O III] 88 μm line flux by 2D Gaussian fitting using `CASA imfit` to the line integrated intensity map. The resultant line flux is 1.06 ± 0.23 Jy km s^{-1}. COS-2987 is spatially resolved in [O III] 88 μm, and its beam-deconvolved size is $0''.88 \times 0''.45$. For the dust continuum, we estimated a conservative upper limit for the total flux density in each band by correcting the noise rms per beam (Section 2.3) for the difference between the beam and object sizes (e.g., T. Hashimoto et al. 2023b). We here assumed that the size of the dust emission region equals that of the [O III] 88 μm emission. We applied the CMB correction in the same manner as for the five clumps (Section 4.1.1). The 3σ upper limits on the dust continuum flux densities are shown in Table 2.

4.2. IRX–β Relation

We investigate the relation between the infrared excess (IRX $= \log(L_{\rm IR}/L_{\rm UV})$, where $L_{\rm IR}$ and $L_{\rm UV}$ represent the UV and infrared luminosities, respectively) and $\beta_{\rm UV}$ to discuss whether the observed red $\beta_{\rm UV}$ and nondetection of the dust continuum are naturally explained with commonly used dust attenuation curves.

The UV slope of COS-2987 was measured by fitting the NIRCam F115W, F150W, and F200W flux densities (Section 4.1) with an exponential function: $f_\lambda \propto \lambda^{\beta_{\rm UV}}$. These NIRCam bands sample the rest-frame wavelengths from 1300–2850 Å that are almost identical to the wavelength definition from D. Calzetti (2001). The UV luminosity is defined as $L_{\rm UV} = \lambda L_\lambda$ at $\lambda = 1600$ Å. We estimated $L_{\rm UV}$ from the F115W flux density. The IR luminosity $L_{\rm IR}$ was estimated by fitting the CMB-corrected ALMA Band 5, 6, and 8 flux densities (Section 4.1) with the modified blackbody assuming the dust temperature of $T_{\rm d} = 50$ K and emissivity index of $\beta_{\rm d} = 2.0$. Because the dust continuum is not detected in any bands, we estimated 3σ upper limits of $L_{\rm IR}$ for the multiple clumps.

Figure 6 shows the IRX and $\beta_{\rm UV}$ of mN, mS, sE, sN1, and the total system (Total) with the circle, square, diamond, pentagon, and star symbols, respectively. For sN2, neither IRX nor $\beta_{\rm UV}$ can be estimated because of nondetection in F115W, F150W, F200W, and ALMA continuum bands. COS-2987, as a whole (Total), shows $\beta_{\rm UV} = -1.9 \pm 0.3$. Our measurement is bluer than that of the previous work ($\beta_{\rm UV} \sim -1.1$; R. Smit et al. 2018), which may be due to the difference of the instruments and filters used. The upper limit on the IRX of Total, <0.39 (3σ), is significantly higher than that obtained in the previous work (R. Smit et al. 2018). This is due to our conservative upper limits on the ALMA continuum fluxes taking into account the aperture area (Section 4.1). Looking at each clump, sN1 and sE have notably blue UV slope of $\beta_{\rm UV} = -2.2 \pm 0.3$ and -2.7 ± 0.8, respectively, while mN and mS are as red as $\beta_{\rm UV} \sim -1.6$. This UV color difference can also be visually confirmed in the pseudo-color image superposed in Figure 6. This may suggest patchy stellar-and-dust geometry (A. L. Faisst et al. 2017; Y. Tamura et al. 2023). Alternatively, sN1 and sE may be satellite galaxies with different dust properties compared to the main clumps.

The IRX–$\beta_{\rm UV}$ relations are connected with attenuation curves because of the energy balance between absorption and reradiation by dust (G. R. Meurer et al. 1999). There are two types of frequently used "canonical" relations: one for local starbursts proposed by G. R. Meurer et al. (1999) that implicitly includes the Calzetti dust attenuation curve (D. Calzetti et al. 2000; R. J. Bouwens et al. 2016a), and another expected with the SMC attenuation curve (M. L. Prevot et al. 1984; K. D. Gordon et al. 2003). We hereafter refer them to the Calzetti and SMC relations for convenience. They are shown by the thin curves in Figure 6, where we followed the calculation of R. J. Bouwens et al. (2016a). We note that these canonical relations assume that the

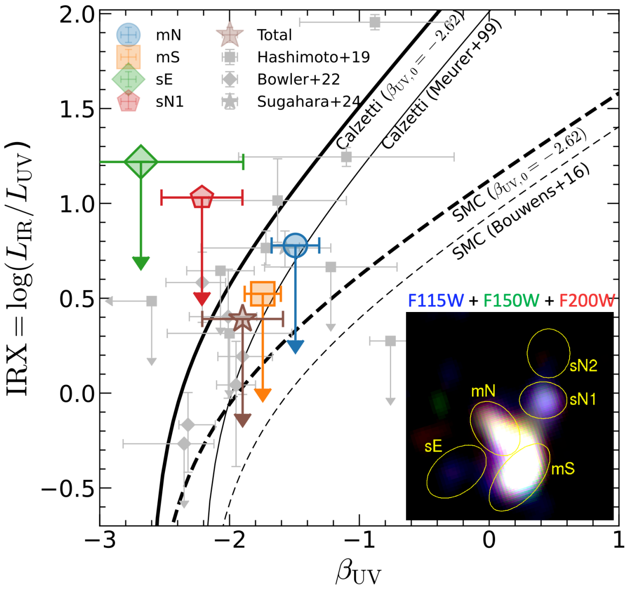

Figure 6. IRX–$\beta_{\rm UV}$ diagram. The mN, mS, sE, sN1 clumps, and total system are shown by the circle, square, pentagon, diamond, and star symbols, respectively. Their IRX measurements are 3σ upper limits as represented by the arrows. The gray square, diamond, and star symbols show $6.5 < z < 9.1$ galaxies taken from T. Hashimoto et al. (2019), R. A. A. Bowler et al. (2022), and Y. Sugahara et al. (2025), respectively. All of the IRX values from the literature are corrected for $T_{\rm d} = 50$ K and $\beta_{\rm d} = 2.0$. Thin solid and dashed lines correspond to the canonical relations assuming the Calzetti and SMC dust attenuation curves (G. R. Meurer et al. 1999; R. J. Bouwens et al. 2016a), respectively. Thick lines are the same but modified with $\beta_{\rm UV,0} = -2.62$ (N. A. Reddy et al. 2018; see the text). The inset panel shows an F115W + F150W + F200W pseudo-color image with the apertures for the multiple clumps.

intrinsic UV slope without the dust attenuation is $\beta_{\rm UV,0} = -2.23$. High-redshift galaxies tend to have bluer $\beta_{\rm UV,0}$ due to the young ages, low metallicities, and binary interactions (C. C. Steidel et al. 2014, 2016; N. A. Reddy et al. 2018). We then modified the canonical relations so that they have $\beta_{\rm UV,0} = -2.62$ (N. A. Reddy et al. 2018; Y. Sugahara et al. 2025), which are shown by the bold curves in Figure 6. In COS-2987, mN, mS, and Total prefer the SMC relation to the Calzetti relation. While the Calzetti relation can explain the measurements in COS-2987 if $\beta_{\rm UV,0}$ is redder than −2.2, this possibility is rejected in our SED fitting analysis (Section 4.3).

In Figure 6 we also plot spectroscopically confirmed galaxies at $6.5 < z < 9.1$ from T. Hashimoto et al. (2019), R. A. A. Bowler et al. (2022), and Y. Sugahara et al. (2025) where we corrected the literature data for the dust temperature difference. Most of the galaxies whose dust continuum emission is detected follow the Calzetti relation with $-2.6 < \beta_{\rm UV,0} < -2.2$ (see also T. Hashimoto et al. 2019; R. A. A. Bowler et al. 2022; Y. Sugahara et al. 2025). On the other hand, as can be seen in COS-2987, steeper attenuation curves including the SMC curve are favored in stacking analyses of UV-selected galaxies at $2 \lesssim z \lesssim 5$ (N. A. Reddy et al. 2018; Y. Fudamoto et al. 2020; but see also the opposite conclusion in J. Álvarez-Márquez et al. 2016, 2019; R. A. A. Bowler et al. 2024). There seems to be a diversity in the dust properties of high-redshift galaxies. The difference between the galaxies on the Calzetti and SMC IRX–$\beta_{\rm UV}$ relations should be statistically investigated as a future work.

4.3. SED Fitting

We performed SED fitting analyses for the multiple clumps in COS-2987 with the `PANHIT` code (T. Hashimoto et al. 2018; Y. Tamura et al. 2019; K. Mawatari et al. 2020a, 2020b). The `PANHIT` combines the stellar, nebular, and dust emission SEDs by implementing the models of G. Bruzual & S. Charlot (2003), A. K. Inoue (2011), and the modified blackbody radiation, respectively. The [O III] 88 μm line flux is modeled with the empirical scaling relation from SFR (A. K. Inoue et al. 2014b). For the stellar models, we assumed the Chabrier IMF (G. Chabrier 2003). Fluxes at rest-frame wavelengths equal to or shorter than Lyα are attenuated by the intergalactic medium, following the analytic model of A. K. Inoue et al. (2014a).

We simultaneously fit the NIRCam, ALMA continuum flux densities, NIRSpec, and ALMA emission-line fluxes. We excluded the [O III] 4960Å and [O III] 4364 Å line fluxes. The [O III] 4960Å flux degenerates with the [O III] 5008 Å flux in the modeling because their ratio is fixed (≃3; P. J. Storey & C. J. Zeippen 2000). Combined with the [O III] 5008 flux, the [O III] 4364 flux is sensitive to the electron temperature $T_{\rm e}$ (D. E. Osterbrock & G. J. Ferland 2006; B. T. Draine 2011). The nebular emission model of A. K. Inoue (2011) assumes $T_{\rm e}$ as a function of metallicity, which limits the reproducibility of the temperature-sensitive line flux in galaxies that deviate from average physical condition. We performed detailed line diagnostics including the [O III] 4364 Å line of COS-2987 in our companion paper (M. Usui et al. 2025). The measured flux of the [O II] 3727,3730 Å doublet was summed so as to match the model that does not resolve the doublet (A. K. Inoue 2011). The [O III] 88 μm line flux was used only for the total photometry (Total) because it is not spatially resolved in ALMA Band 8. On the other hand, the upper limits on the ALMA Band 5, 6, and 8 flux densities were measured for each clump (Section 4.1).

In the SED fitting, we fixed the redshifts for the clumps (Section 4.1). Star formation history (SFH) was assumed to be constant because it was not constrained in our trial with the delayed-τ model. Free parameters are dust attenuation A_V, stellar age, metallicity Z, and escape fraction of ionizing photons $f_{\rm esc}$. Their fitting ranges are $0 \leqslant A_V \leqslant 2$, 1 Myr < age < the cosmic age at $z = 6.81$, $0.0001 \leqslant Z \leqslant 0.05$ ($0.005 Z_\odot \leqslant Z \leqslant 2.5 Z_\odot$), and $0 \leqslant f_{\rm esc} \leqslant 1$. We used the SMC dust attenuation curve that is preferred in the IRX–$\beta_{\rm UV}$ relation (Section 4.2). Dust temperature and emissivity index in the modified blackbody are assumed to be $T_{\rm d} = 50$ K and $\beta_{\rm d} = 2.0$. We assumed the same A_V for the nebular emission lines and stellar continua (e.g., D. K. Erb et al. 2006; D. Kashino et al. 2013).

The best-fit model for the whole system (Total) is shown by the brown spectrum and crosses in Figure 7. We can see that the model reasonably reproduces the all observed measurements. The significant F356W excess, $\beta_{\rm UV} \sim -2$, and nondetection in ALMA dust continua are explained by combination of very young age (8 Myr) and modest dust attenuation $A_V \sim 0.2$. This consistency is broken if we assume lower dust temperature ($T_{\rm d} \leqslant 40$ K) and less steep dust emissivity index ($\beta_{\rm d} \leqslant 1.5$).

The best-fit models for the two bright main clumps mN and mS are shown by the blue and orange spectra and crosses in Figure 7. The observed SEDs are well reproduced, and there are similar trends as in Total: the young age, modest dust

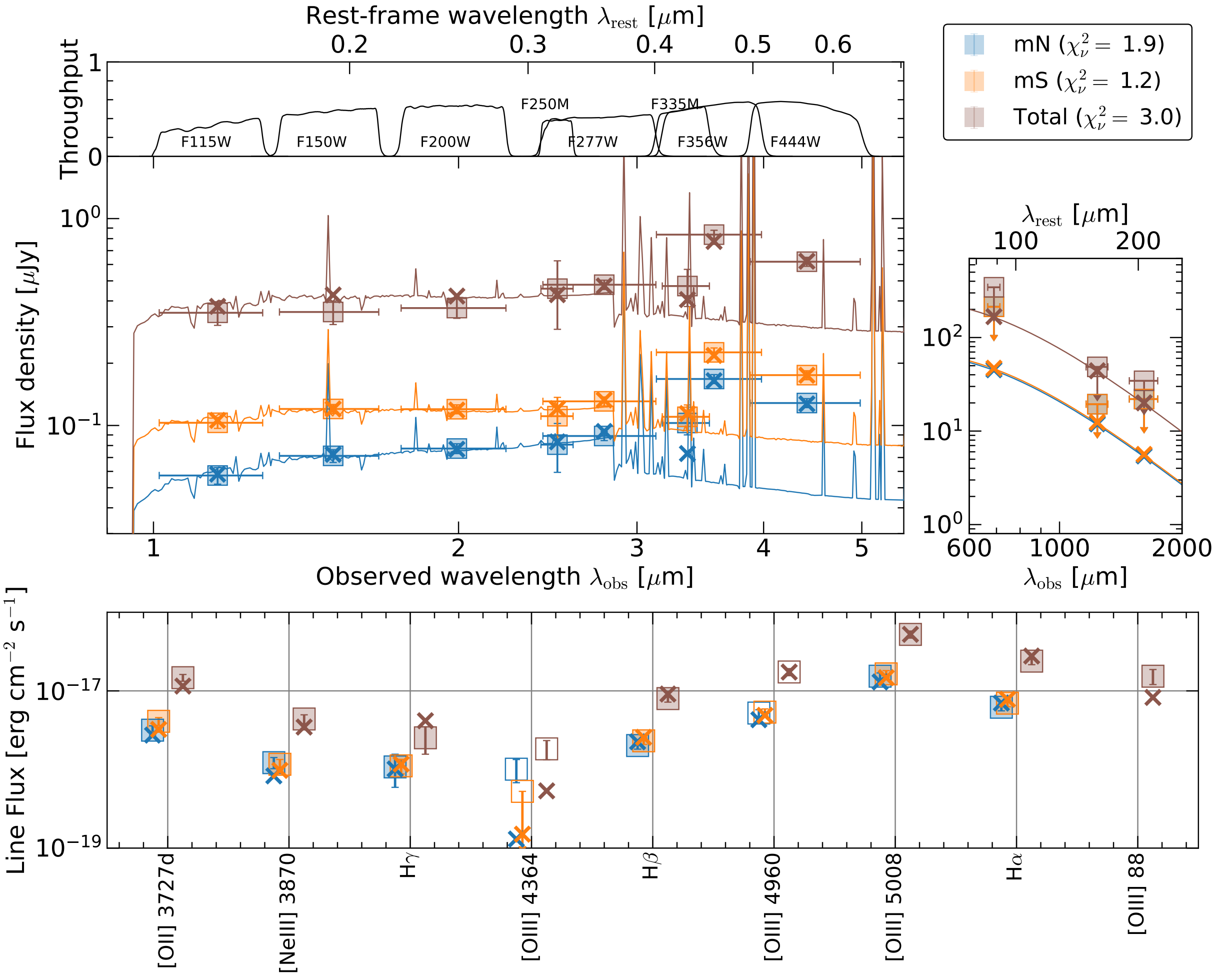

Figure 7. The observed SEDs and the best-fit models for mN, mS, and Total expressed by blue, orange, and brown symbols, respectively. In the top-left panel, squares show the observed NIRCam flux density while the lines and crosses correspond to the best-fit model spectra and their filter-convolved flux density. The top-right panel shows the same but for the ALMA dust continua. In the bottom panel, the squares and crosses correspond to the observed and best-fit model line fluxes, respectively. The label "[O II] 3727d" means sum of the [O II] 3727,3730 Å doublet flux. We also show the [O III] 4364 Å and [O III] 4960 Å lines that were actually not used in the SED fitting. ALMA [O III] 88 μm flux is shown only for the total photometry (Total) because of its coarse spatial resolution.

attenuation, and high emission-line EWs. Their [O III] 5008 Å EWs are as high as 1000–2000 Å in the rest frame, which are comparable to the highest values observed at $5 < z < 7$ (J. Matthee et al. 2023).

The fitting results for the fainter subclumps sE and sN1 are shown in the left and right panels of Figure 8, respectively. Unfortunately, the best-fit solution for sN2 is unreliable due to the limited number of detections in its observed SED. For sE, we failed to obtain the reasonable solution even though this clump has five and four detections in NIRCam and NIRSpec, which is enough to constrain the SED. The minimum χ^2 model is shown by the black spectrum in Figure 8. The observed SED of sE is very different from Total, mN, and mS in extremely blue $\beta_{\rm UV}$ and a break between F200W and F277W flux densities. We then attempted fitting combining two SED models with distinct ages as performed in T. Hashimoto et al. (2018) and Y. Tamura et al. (2019): old stellar population with the Balmer break in F277W and young population with blue $\beta_{\rm UV}$ and strong nebular emission lines. This approach resulted in successful reproduction of the observed SED, as shown by the green solid spectrum and crosses in the left panel of Figure 8. The old and young component models are also shown by thin dashed and solid spectra, respectively.

The situation for sN1 is similar to that of sE, although the failure of the single-component fit is less severe. In the right panel of Figure 8, the black solid spectrum and crosses correspond to the best-fit model in the single-component fitting, which does not perfectly reproduce the blue UV slope. The two-component model (old + young), shown by the red solid spectrum and crosses, yields a slightly better fit and is moderately preferred over the single-component model.

While the SEDs of the main clumps (mN, mS, and Total) are reasonably well explained by the single-component fitting as described above, the presence of underlying old stellar populations cannot be ruled out, as long as their contribution to the observed SEDs is negligible. We performed the two-component SED fitting to the main clumps to evaluate upper limits of their stellar masses. We found that the inclusion of old stellar populations, which could increase the total stellar mass by a factor of 3–10, cannot be ruled out (Section 4.4). Such hidden old stellar populations in high-z star-forming galaxies are also suggested in previous works to explain the

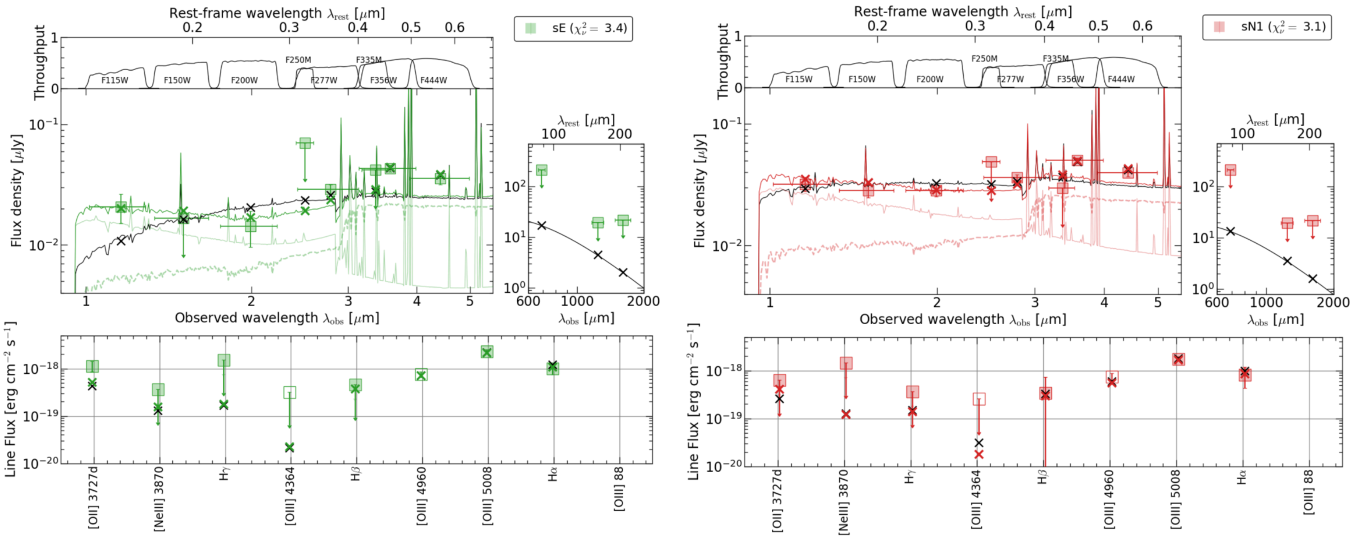

Figure 8. The observed SEDs and the best-fit models for sE (left panels) and sN1 (right panels). The two types of the fitting results are shown for each clump: single-component fitting (black solid spectrum and crosses) and old + young two-components fitting (colored solid spectrum and crosses). In the latter fitting, the old and young models are shown by thin dashed and solid spectra, respectively.

dust formation (T. Hashimoto et al. 2019; Y. Tamura et al. 2019; Y. W. Ren et al. 2025).

4.4. Physical Properties

In Table 3, we summarize the physical quantities of individual clumps, where almost all of the quantities could not be derived for sN2 due to the small numbers of detected bands and lines. The uncertainties associated with the SED fit parameters were derived by the MC iterations of the fitting (K. Mawatari et al. 2020a, 2020b). Figure 9 shows MC probability distribution for each clump as a function of each parameter in the SED fitting.

The dust attenuations are well constrained as $A_V = 0.2$–0.3 for mN, mS, Tot, and $A_V \approx 0$ for sE and sN1. We also estimated A_V from the Hα and Hβ fluxes spatially integrated within each clump (Table 3; Section 3.3) to find that they are consistent with the SED fit results within the uncertainties. The main clumps (mN, mS, and Total) have very young stellar ages of 5–10 Myr, although the presence of older stellar populations with ages of $\gtrsim$100 Myr cannot be ruled out, as discussed in Section 4.3. In contrast, the subclumps (sE and sN1) require a more substantial population of $\gtrsim$100 Myr old stars, such that the contributions from the old and young components become comparable in their SEDs (Figure 8 and Table 3).

The balance between the young stellar (+nebular) component producing strong emission lines and the older stellar populations is reflected in the EWs of rest-optical emission lines (E. M. Levesque & C. Leitherer 2013; E. Telles & J. Melnick 2018). We measured the rest-frame EW (EW$_0$) of each line of each clump using the line flux observed by NIRSpec IFS (Table 2) and the continuum flux density estimated from the best-fit model spectrum (Section 4.3). The EW$_0$ measurements are summarized in Table 3 and shown in Figure 10. In the Balmer and [O III] 5008 Å, 4960Å lines that are sensitive to SFR, the subclumps have lower EWs than the main clumps. This trend likely reflects a larger contribution from older stellar populations in the subclumps, diluting the emission-line EWs.

The stellar masses (M_*) of individual clumps range 1–5 × $10^8\,M_\odot$, with large uncertainty caused by possible hidden old stellar populations for the main clumps. The SFR output by `PANHIT` corresponds to the SFR at the observed epoch, assuming a constant SFH, which we refer to as SFR (SED). COS-2987, in total, has the SFR(SED) as high as $80\,M_\odot\,{\rm yr}^{-1}$ that are mainly owed by mN and mS. For comparison with previous works, we also estimated two types of SFRs: SFR estimated from the observed UV and Hα luminosities ($L_{\rm UV}$ and $L_{\rm H\alpha}$), which we refer to SFR(UV) and SFR(Hα), respectively. The $L_{\rm UV}$ was estimated from the NIRCam F115W flux density in the same manner as in Section 4.2. The $L_{\rm UV}$ and $L_{\rm H\alpha}$ were both corrected for the dust attenuation with the best-fit A_V from the SED fitting and from the Balmer decrement, respectively. We adopted the conversion factors from UV and Hα luminosities to SFR(UV) and SFR(Hα) for low-metallicity galaxies following the prescriptions of R. L. Theios et al. (2019) and A. E. Shapley et al. (2023). It is known that the SFR(Hα) and SFR(UV) roughly trace 10 Myr and 100 Myr scale star formation, respectively (e.g., R. C. Kennicutt & N. J. Evans 2012; D. Calzetti 2013). The SFR(SED) measurements are comparable to the SFR(Hα).

Figure 11 shows COS-2987 in M_* versus SFR space, where the SFR(UV) and SFR(Hα) are used in the left and right panels, respectively. We also superpose the tight relation, "main sequence" of star-forming galaxies, at $6 \lesssim z \lesssim 7$ from the literature (J. S. Speagle et al. 2014; B. Salmon et al. 2015; J. W. Cole et al. 2025). J. W. Cole et al. (2025) estimated 10 and 100 Myr averaged SFRs from CEERS (S. L. Finkelstein et al. 2022; M. B. Bagley et al. 2023; S. L. Finkelstein et al. 2025), which roughly correspond to the SFR(Hα) and SFR (UV), respectively. B. Salmon et al. (2015) investigated SFR (UV) using the data from the Cosmic Assembly Near-infrared Deep Extragalactic Legacy Survey (N. A. Grogin et al. 2011; A. M. Koekemoer et al. 2011). J. S. Speagle et al. (2014) compiled various existing data to obtain the main sequence as a function of the cosmic time. Ignoring the uncertainties in the M_* and SFR measurements, the main clumps (mN, mS, and Total) lie about 2σ above the previously established main sequence in both SFR(UV) and SFR(Hα), where σ denotes the

Table 3
Physical Quantities from the Multiwavelength Data

	mN	mS	sE	sN1	sN2	Total
SED fitting results[a]						
Dust A_V(SED) [mag]	$0.28^{+0.03}_{-0.04}$	$0.20^{+0.02}_{-0.02}$	$0.00^{+0.02}_{-0.00}$	$0.00^{+0.05}_{-0.00}$	⋯	$0.20^{+0.03}_{-0.03}$
Age [Myr]	$5.2^{+1.7}_{-1.0}$	$8.3^{+1.6}_{-1.6}$	$1.4^{+0.4}_{-0.4}$ (young)	$6.9^{+25.1}_{-5.9}$ (young)	⋯	$8.3^{+2.0}_{-1.2}$
			$160.9^{+207.7}_{-50.2}$ (old)	$101.5^{+18.1}_{-0.0}$ (old)		
Escape fraction $f_{\rm esc}$(SED) [%]	$0.0^{+0.0}_{-0.0}$	$0.0^{+8.7}_{-0.0}$	$0.0^{+9.7}_{-0.0}$	$10.0^{+30.8}_{-10.0}$	⋯	$0.0^{+0.0}_{-0.0}$
Metallicity Z(SED) [$Z_\odot$]	$0.40^{+0.00}_{-0.19}$	$0.40^{+0.00}_{-0.00}$	$0.40^{+0.47}_{-0.00}$	$0.40^{+0.60}_{-0.20}$	⋯	$0.40^{+0.00}_{-0.18}$
Stellar mass M_* [$10^8\ M_\odot$]	$1.12^{+4.46}_{-0.12}$[b]	$1.72^{+3.54}_{-0.18}$[b]	$3.22^{+1.95}_{-0.70}$	$2.98^{+0.71}_{-0.70}$	⋯	$6.12^{+54.52}_{-0.45}$[b]
SFR(SED) [$M_\odot$ yr^{-1}]	$21.6^{+1.3}_{-2.2}$	$21.5^{+1.2}_{-0.8}$	$6.9^{+4.4}_{-0.1}$	$2.4^{+14.6}_{-0.1}$	⋯	$76.6^{+3.8}_{-5.1}$
Properties from line diagnostics						
Dust $A_{\rm V}$(BD) [mag][c]	$0.28^{+0.38}_{-0.28}$	$0.22^{+0.35}_{-0.22}$	⋯	$0.0^{+1.4}_{-0.0}$	⋯	$0.23^{+0.32}_{-0.23}$
SFR(Hα) [$M_\odot$ yr^{-1}]	8.9 ± 2.6	9.5 ± 2.5	1.1 ± 0.3	$0.9^{+1.1}_{-0.9}$	⋯	32.8 ± 8.2
Metallicity Z(R3) [$Z_\odot$][d]	$0.10^{+0.03}_{-0.02}$	$0.08^{+0.03}_{-0.02}$	⋯	$0.05^{+0.23}_{-0.05}$	⋯	$0.07^{+0.03}_{-0.02}$
Ionizing parameter log($U_{\rm ion}$)	$-2.71^{+0.07}_{-0.08}$	$-2.78^{+0.06}_{-0.08}$	⋯	>-2.99	⋯	-2.83 ± 0.06
Rest-frame EWs of emission lines						
EW$_0$([O II] 3727d) [Å]	189.4 ± 25.6	162.6 ± 18.5	253.0 ± 63.5	<94.4	⋯	164.1 ± 16.2
EW$_0$([Ne III] 3870) [Å]	81.7 ± 13.3	48.3 ± 7.3	<62.4	<173.5	⋯	51.2 ± 6.7
EW$_0$(Hγ) [Å]	104.9 ± 47.2	64.6 ± 13.6	<365.9	<62.0	⋯	41.3 ± 15.8
EW$_0$([O III] 4364) [Å]	99.2 ± 32.5	<30.9	<76.7	<44.1	⋯	30.2 ± 8.3
EW$_0$(Hβ) [Å]	251.1 ± 25.1	165.6 ± 16.6	<124.4	66.7 ± 76.7	⋯	160.5 ± 15.9
EW$_0$([O III] 4960) [Å]	668.8 ± 66.9	391.9 ± 39.2	189.6 ± 27.1	141.5 ± 23.4	⋯	357.5 ± 36.9
EW$_0$([O III] 5008) [Å]	2016.9 ± 201.7	1229.8 ± 123.0	590.1 ± 59.0	343.8 ± 34.4	⋯	1098.8 ± 114.0
EW$_0$(Hα) [Å]	1580.6 ± 158.1	974.1 ± 97.4	446.5 ± 109.8	294.8 ± 138.1	⋯	938.3 ± 92.8
Others						
$M_{\rm UV}$ [mag][e]	−19.9 ± 0.1	−20.5 ± 0.1	−18.8 ± 0.3	−19.3 ± 0.1	>-18.3	$-21.9^{+0.2}_{-0.1}$
SFR(UV) [$M_\odot$ yr^{-1}]	8.6 ± 1.5	11.0 ± 1.3	0.9 ± 0.3	1.4 ± 0.3	⋯	37.4 ± 7.0
log($\xi_{\rm ion}$ [Hz erg^{-1}])	$25.38^{+0.13}_{-0.18}$	$25.30^{+0.11}_{-0.15}$	$25.45^{+0.14}_{-0.20}$	$25.17^{+0.32}_{-\infty}$	⋯	$25.31^{+0.12}_{-0.16}$
Escape fraction $f_{\rm esc}$(C24) [%][f]	$0.8^{+1.4}_{-0.8}$	$2.6^{+3.4}_{-2.6}$	⋯	⋯	⋯	$5.2^{+8.9}_{-5.2}$

Notes. The 3σ upper limits are given for nondetections.

[a] The fitting results with the two-component model (old and young) are shown for sE and sN1, while the one-component fits are applied for the other clumps.

[b] The 1σ upper errors for the stellar mass of mN, mS, and Total are given from the two-component fits to avoid underestimating the stellar mass (see the text).

[c] Dust attenuation A_V from the Balmer decrement (Hα/Hβ) measurements. The physical quantities below in the table are estimated from the dust attenuation-corrected line fluxes.

[d] Metallicity $12 + \log({\rm O/H})$ from the R3 index is estimated following M. Hirschmann et al. (2023). In this table they are expressed in $Z\,[Z_\odot]$ assuming $12 + \log({\rm O/H})_\odot = 8.69$.

[e] Absolute UV magnitudes are estimated from the NIRCam F115W fluxes where no dust attenuation correction is applied.

[f] An analytic formulae of N. Choustikov et al. (2024) is used to estimate the escape fractions of ionizing photons ($f_{\rm esc}$).

1σ uncertainty of the main-sequence relation. However, since the stellar masses of the main clumps could be significantly larger than their face values, we cannot definitively conclude that they are in a starburst phase relative to main-sequence galaxies. The subclumps sE and sN1 are on or below the main sequence.

The ratio of SFR(Hα) and SFR(UV) is considered as the star-burstiness because of the difference in their timescales (e.g., D. R. Weisz et al. 2012; M. Sparre et al. 2017; H. Atek et al. 2022; Y. Asada et al. 2024; R. Endsley et al. 2025). In COS-2987, all of the clumps have the ratios of ∼1, suggesting that these clumps are not necessarily undergoing a starburst phase.

The ionizing photon production efficiency, $\xi_{\rm ion}$, is the number of ionizing photons produced per unit UV luminosity density (B. E. Robertson et al. 2013). This quantity is important to assess the ionizing budget from star-forming galaxies, particularly in the reionization era (e.g., B. E. Robertson et al. 2013; R. J. Bouwens et al. 2016b; J. Matthee et al. 2017). We followed J. Álvarez-Márquez et al. (2024) to estimate $\xi_{\rm ion}$ of each clump from the observed Hα luminosity ($L_{\rm H\alpha}$ [erg s^{-1}]) and UV luminosity density ($L_{\nu,\rm UV}$ [erg s^{-1} Hz^{-1}]), assuming ionizing photon escape fraction $f_{\rm esc} = 0$. The $L_{\nu,\rm UV}$ was estimated from the NIRCam F115W flux density. The $L_{\rm H\alpha}$ and $L_{\nu,\rm UV}$ were corrected for dust attenuation A_V. We assumed the same A_V for the Hα nebular emission and UV stellar continuum (c.f., D. K. Erb et al. 2006; D. Kashino et al. 2013). The estimated $\xi_{\rm ion}$ values are shown in Figure 12 along with other galaxies at $6 \lesssim z \lesssim 12$ (J. Álvarez-Márquez et al. 2024 and references therein; T. Y.-Y. Hsiao et al. 2024; J. Álvarez-Márquez et al. 2025; J. A. Zavala et al. 2025). The $\xi_{\rm ion}$ of mN, mS, sE, sN1, and Total are distributed around the canonical value of $\log(\xi_{\rm ion}\,[{\rm Hz\ erg^{-1}}]) = 25.2$ (B. E. Robertson et al. 2013) and are comparable to the other galaxies. Our measurements are roughly consistent with the redshift evolution reported by J. Matthee et al. (2017), and also with the prediction from the FirstLight simulation ($\log(\xi_{\rm ion}\,[{\rm Hz,\ erg^{-1}}]) \sim 25.3$ at $z = 7$; D. Ceverino et al. 2019).

From the SED fitting, COS-2987 prefers zero escape fraction of the ionizing photons ($f_{\rm esc} \sim 0$; Figure 9). Because the escape fraction is intricately related to various physical quantities, a more careful estimation is needed. We used the

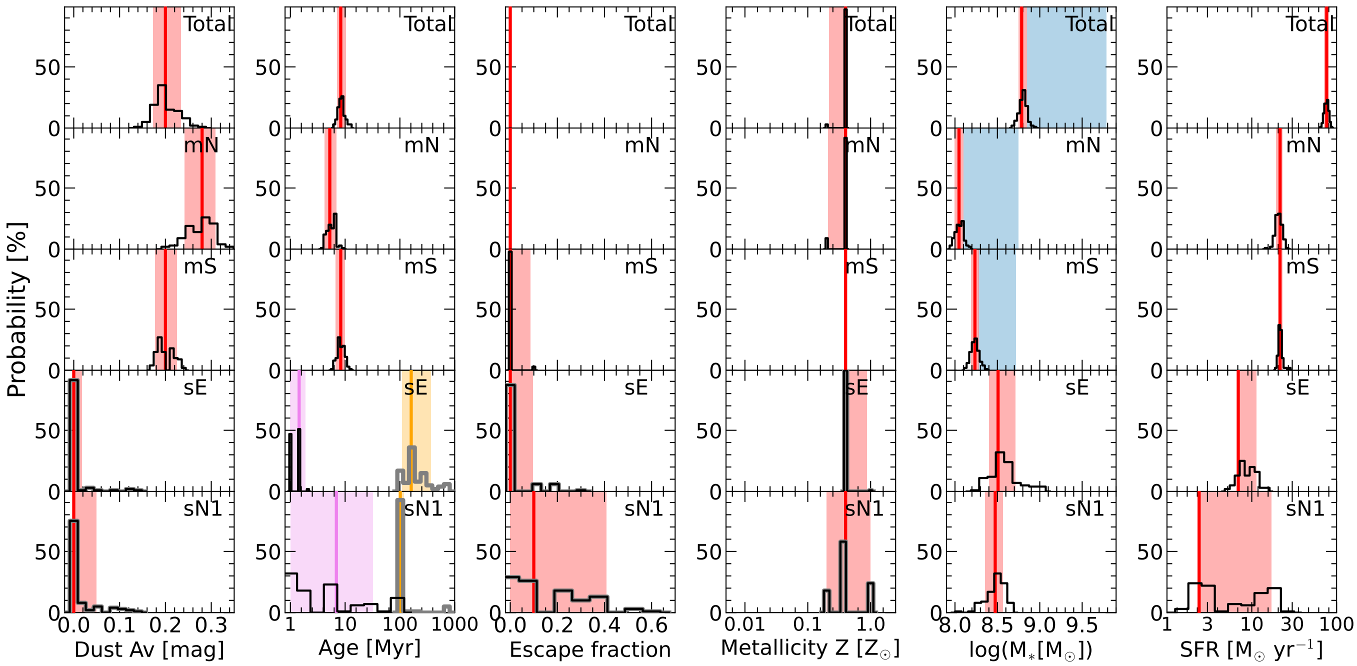

Figure 9. Probability distributions of physical quantities for the all clumps (black histogram) except for sN2. These are derived from 100 MC iterations of the SED fitting (Section 4.3; K. Mawatari et al. 2020a, 2020b). In each panel, vertical solid lines and shaded areas indicate the best-fit quantity and its 1σ uncertainty. For sE and sN1, there are two age solutions corresponding to the young and old components. In the panels of stellar mass of the main clumps (mN, mS, and Total), blue shaded regions are also shown, which correspond to 1σ uncertainties taking account of hidden old stellar populations by the two-component fitting (Section 4.3).

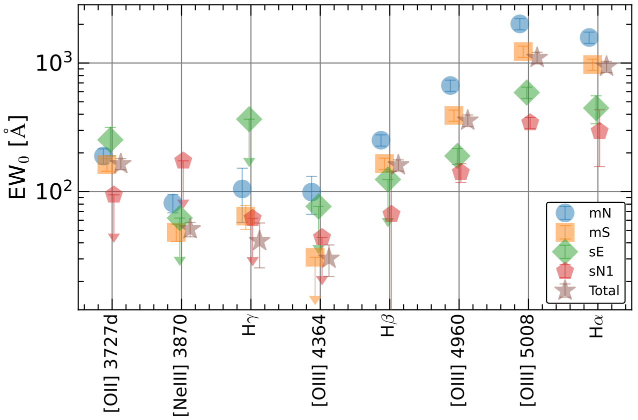

Figure 10. The rest-frame EWs of the emission lines from the multiple clumps in COS-2987.

analytic formulae of N. Choustikov et al. (2024), who comprehensively investigate relations between $f_{\rm esc}$ and various observable quantities. Their formulae require six measurements of $\beta_{\rm UV}$, dust extinction $E(B\,-\,V)$, $\log(L_{\rm H\beta})$, UV absolute magnitude $M_{\rm UV}$, O32 index, and R23 index = ([O III] 4960,5008 Å+[O II] 3727,3730 Å)/Hβ, which allows us to evaluate $f_{\rm esc}$ of mN, mS, and Total. We obtain escape fractions of $f_{\rm esc} \approx 1\%$–5%, but they are not significantly different from zero given the uncertainties. (Table 3).

5. Conclusions: A Comprehensive View of COS-2987

We here discuss the nature of COS-2987 taking into account all of the results in the above sections. The NIRSpec IFS data revealed the morphology and kinematics: the five clumps in the complex velocity field support the interpretation that this system is not a rotation-dominated disk (Section 3.2). This seems inconsistent with the previous ALMA studies reporting a rotating disk (R. Smit et al. 2018; A. C. Posses et al. 2023). As mentioned by A. C. Posses et al. (2023), their ALMA [C II] 158 μm observations may lack the spatial resolution (the beam size $=0\farcs44 \times 0\farcs35$) and SNR ($\sim$7) to distinguish a rotating disk and merger, compared to the requirements proposed by F. Rizzo et al. (2022; i.e., SNR $\gtrsim$ 10 and more than three independent resolution elements).

On the other hand, the difference in kinematics between our JWST and previous ALMA observations is not necessarily contradictory, because the [O III] 5008 Å and [C II] 158 μm line emissions trace different gas phases, warm ionized ($T \sim 10^4$ K) and cold molecular/neutral ($T \sim 100$ K) gas, respectively (E. Parlanti et al. 2023; S. Arribas et al. 2024; M. Kohandel et al. 2024; F. Rizzo et al. 2024). It is plausible that, in the case of COS-2987, ALMA traces the underlying cold disk, whereas JWST probes the turbulent ionized gas, potentially driven by a merger or supernova feedback. Differences in the apparent gas kinematics depending on the emission-line tracers have also been reported in other high-z galaxies. For instance, in the case of MACS1149-JD1 at $z = 9.1$, the ALMA observations of [O III] 88 μm suggested a rotating disk (T. Tokuoka et al. 2022), while the NIRSpec IFS of [O III] 5008 Å indicated a merger (C. Marconcini et al. 2024). MACS0416-Y1 at $z = 8.3$ showed rotational signatures in [C II] 158 μm (T. J. L. C. Bakx et al. 2020), whereas [O III] 88 μm indicated more turbulent, disordered motion (Y. Tamura et al. 2023). Another case is COS-3018 at $z = 6.85$: R. Smit et al. (2018) proposed a rotating disk based on ALMA [C II] 158 μm data, but J. Scholtz et al. (2025) later identified it as a merger based on NIRSpec IFS observations. These examples highlight the importance of carefully considering both the sensitivity and the choice of gas tracers when assessing the morpho-kinematic nature of high-z galaxies.

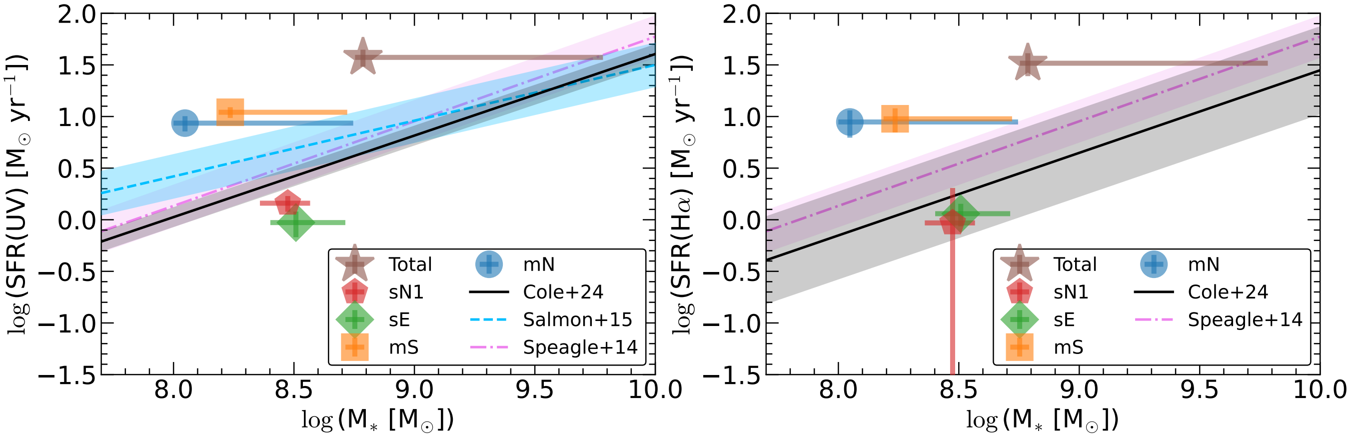

Figure 11. Stellar mass vs. SFR diagram. The SFRs of COS-2987 estimated from the UV and Hα luminosities are shown in the left and right panels. The mN, mS, sN1, and Total clumps are indicated by the circle, square, pentagon and star, respectively. Star formation main sequences from J. W. Cole et al. (2025), B. Salmon et al. (2015), and J. S. Speagle et al. (2014) are shown by solid, dashed, and dotted–dashed lines, respectively. The associated shades correspond to 1σ uncertainty from each literature. We plot 100 and 10 Myr averaged SFRs of $6 < z < 7$ galaxies from J. W. Cole et al. (2025) in comparison with our SFR(UV) and SFR(Hα). The main sequence of B. Salmon et al. (2015) was measured using SFR(UV) of $z \sim 6$ galaxies. J. S. Speagle et al. (2014) compiled various previous works to establish the redshift-dependent main sequence, from which we extract that at $z = 6.81$.

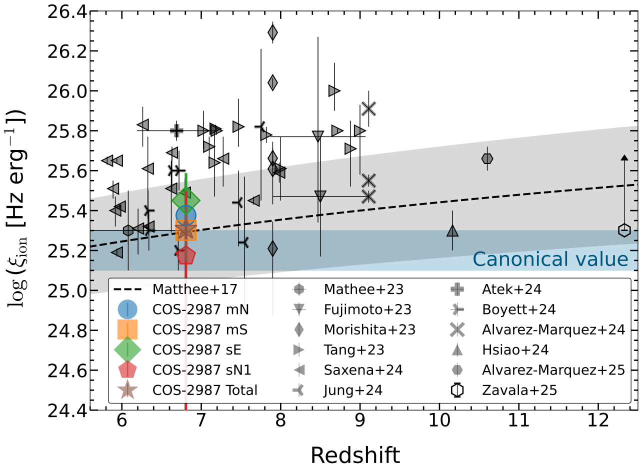

Figure 12. Ionizing photon production efficiency $\xi_{\rm ion}$ as a function of redshift. The mN, mS, sN1, and Total clumps in COS-2987 are represented by the circle, square, pentagon and star, respectively. We also plot galaxies spectroscopically confirmed at $z \gtrsim 6$ with JWST from literature (S. Fujimoto et al. 2023; J. Matthee et al. 2023; T. Morishita et al. 2023; M. Tang et al. 2023; J. Álvarez-Márquez et al. 2024, 2025; H. Atek et al. 2024; K. Boyett et al. 2024; T. Y.-Y. Hsiao et al. 2024; I. Jung et al. 2024; A. Saxena et al. 2024; J. A. Zavala et al. 2025). The blue shaded region shows the canonical value for $\xi_{\rm ion}$ (B. E. Robertson et al. 2013). The black line and gray shaded regions show the redshift evolution of $\xi_{\rm ion}$ and its uncertainty (J. Matthee et al. 2017).

Comparison with simulations can help the understanding of this galaxy. Y. Nakazato et al. (2024) analyzed galaxies at $5.5 \leqslant z \leqslant 9.5$ in the FirstLight simulation (D. Ceverino et al. 2017). They find that about 10% of the simulated galaxies show clumpy morphology in the [O III] 5008 Å emission (i.e., multiple knots in $\sim$10 kpc extent). Interestingly, most of the [O III] 5008 Å bright clumps with the line flux $>10^{-18}$ erg s^{-1} cm^{-2} are formed by major mergers enhancing the tidal compression of gas (e.g., P. Di Matteo et al. 2008; F. Renaud et al. 2014), not by violent disk instability accompanied with the cold gas accretion (e.g., A. Dekel et al. 2009; D. Ceverino et al. 2010). The similarity in the SFR surface density ($\sim 10\,M_\odot$ yr^{-1} kpc^{-2}; Figure 5) and spatial extent ($\sim$10 kpc) between COS-2987 and the simulated clumpy galaxies suggests that the multiple clumps in COS-2987 are also induced by the major merger event. The tidal tail-like structure of sE is also consistent with the merger-induced clumpy galaxies in the simulation. Thus, if COS-2987 is undergoing a major merger, the five observed clumps are naturally explained as a mixture of interacting galaxies and clumps newly formed through tidal gas compression.

The physical properties of COS-2987 provide further insights into its nature. The stellar masses of the clumps are comparable (mass ratio $\sim$1–3:1; Section 4.4) and significantly higher ($\sim 10^8$–$10^9\,M_\odot$) than those of clumps typically formed via violent disk instability ($\sim 10^5$–$10^6\,M_\odot$; e.g., Y. Guo et al. 2015). Such massive and comparable clumps fall within the typical definition of major mergers (e.g., J. M. Lotz et al. 2010; V. Rodriguez-Gomez et al. 2015). Furthermore, the spatially resolved metallicity map reveals a difference in gas-phase metallicity between mN and mS, suggesting different chemical enrichment histories.

An interesting result revealed by NIRSpec high spatial resolution IFS is that the subclumps (sE and sN1) show very different properties compared to the main clumps: dust-free ($A_V \approx 0$), a greater population of old stars with age $\gtrsim$100 Myr (Section 4.4), and significantly different velocities (~ -40 km s^{-1} for sN1; Section 3.2). Such diversity in clump properties has also been observed in other high-redshift merging systems (e.g., S. Arribas et al. 2024; G. C. Jones et al. 2024b, 2024a, 2025; Y. Sugahara et al. 2025). In the case of merger, sN1 may be a "perturber" that is originally a different galaxy and triggers the clumpy starburst in the "host" galaxy. The largest velocity dispersion between sN1 and mN (Section 3.2 and Appendix A) can be explained by their merger. The tail-like morphology of sE naturally evokes a tidal tail stripped from sN1 (Figure 2). Based on the significant blueshift of sN1 with respect to mN, we propose a scenario in which sN1 is colliding into mN from behind, while sE represents a tidal tail that has been stripped during the interaction. This configuration is illustrated schematically in Figure 13. In this scenario, mS and sN2 could be either originally distinct galaxies or merger-induced clumps formed within the main galaxy (mN).

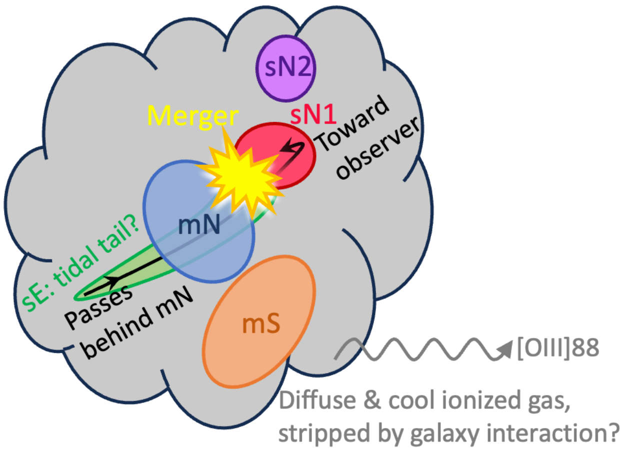

Figure 13. Schematic illustration of the physical picture of COS-2987. The clump sN1 is merging into mN from behind, and sE may be a tidal tail caused by the gravitational interaction. The gray shaded region corresponds to relatively low-density and low-temperature ionized gas emitting the [O III] 88 μm line, which may originate from tidal gas stripping by the merger.

Previous ground-based rest-frame UV spectroscopy detects the Lyα emission line from COS-2987, which indicates the existence of an ionized bubble around this galaxy (N. Laporte et al. 2017). Our rest-frame optical IFS shows the high-ionizing photon production efficiency (Section 4.4). On the other hand, the ionizing photon escape fraction is estimated to be almost zero in mN, mS, and Total (Section 4.4). A possible scenario is that the ionized bubble had already formed before the merger, and the dust formed during the merger made it difficult for the ionizing photons to escape. This idea is supported by potentially complex SFH expected from the coexistence of old and young stellar populations (Section 4.3). Another scenario is that the subclumps with blue UV slope β (Section 4.2) actually have high escape fractions, which cannot be verified with the current data due to the lack of the required measurements (Section 4.4; N. Choustikov et al. 2024). We need deeper IFS observations to distinguish the scenarios.

In the companion paper (M. Usui et al. 2025), we investigate COS-2987 focusing on the doubly ionized oxygen lines, [O III] 4364 Å, [O III] 5008 Å, and [O III] 88 μm. That study suggests the presence of a multiphase ionized gas structures, characterized by distinct combinations of electron temperatures and densities. The [O III] 88 μm line emission originates predominantly from low-temperature and low-density ionized gas. One possible origin of such diffuse and cool ionized gas is tidal stripping of gas from sN1 and mN, induced by the merger supported in this study (Figure 13). We speculate that the dispersal of gas into extended, diffuse regions may suppress the star-burstiness of the clumps estimated from the SFR(Hα)/SFR(UV) ratio (Section 4.4). Future high spatial resolution ALMA observations resolving the [O III] 88 μm morphology at a comparable scale to JWST would provide to be a crucial insight into the physical origin and distribution of the diffuse and cooler ionized gas.

Acknowledgments

We are grateful to Nicholas Choustikov, Yuki Isobe, Nario Kuno, and Hide Yajima for useful discussions. This paper makes use of the following ALMA data: ADS/JAO.ALMA #2018.1.00429.S, #2018.1.01551.S, #2015.1.01111.S, and #2018.1.01359.S. ALMA is a partnership of ESO (representing its member states), NSF (USA) and NINS (Japan), together with NRC (Canada), NSC and ASIAA (Taiwan), and KASI (Republic of Korea), in cooperation with the Republic of Chile. The Joint ALMA Observatory is operated by ESO, AUI/NRAO, and NAOJ. This work has made use of data from the European Space Agency (ESA) mission Gaia (https://www.cosmos.esa.int/gaia), processed by the Gaia Data Processing and Analysis Consortium (DPAC, https://www.cosmos.esa.int/web/gaia/dpac/consortium). Funding for the DPAC has been provided by national institutions, in particular the institutions participating in the Gaia Multilateral Agreement. The Gaia data are retrieved from the JVO portal (http://jvo.nao.ac.jp/portal) operated by the NAOJ. This research has made use of NASA's Astrophysics Data System. Data analysis was in part carried out on the Multiwavelength Data Analysis System operated by the Astronomy Data Center (ADC), National Astronomical Observatory of Japan. K.M. acknowledges the Waseda University Grant for Special Research Projects (project No. 2025C-484) and the Japan Society for the Promotion of Science (JSPS) KAKENHI grant No. 20K14516. K.M. and A.K.I are supported by JSPS KAKENHI grant No. 23H00131. K.M. and T.H. are supported by JSPS KAKENHI grant No. 22H01258. T.H. was supported by Leading Initiative for Excellent Young Researchers, MEXT, Japan (HJH02007) and by JSPS KAKENHI grant Nos. 23K22529 and 25K00020. A.K.I. and Y.S. are supported by NAOJ ALMA Scientific Research grant No. 2020-16B. J.A.-M., L.C., and S.A. acknowledge support by grants PIB2021-127718NB-100 from the Spanish Ministry of Science and Innovation/State Agency of Research MCIN/AEI/10.13039/501100011033 and by "ERDF A way of making Europe." L.C. acknowledges financial support from Comunidad de Madrid under Atracción de Talento grant 2018-T2/TIC-11612. Y.N. is supported by JSPS KAKENHI grant No. 23KJ0728 and a JSR fellowship. Y.W.R. was supported by JSPS KAKENHI grant No. 23KJ2052. Y.F. acknowledges supports from JSPS KAKENHI grant Nos. JP22K21349 and JP23K13149. M.H. is supported by Japan Society for the Promotion of Science (JSPS) KAKENHI grant No. 22KJ1598. A.C.G. acknowledges support by JWST contract B0215/JWST-GO-02926. C.B.-P. acknowledge support by grant CM21_CAB_M2_01 from the Program "Garantía Juveníl" from the "Comunidad de Madrid" 2021. Y.T. is supported by JSPS KAKENHI grant No. 22H04939. M.P.S. acknowledges funding support from the Ramón y Cajal program of the Spanish Ministerio de Ciencia e Innovación (RYC2021-033094-I).

Facilities: JWST (STIS), ALMA.

Software: jdaviz (JDADF Developers et al. 2023), astropy (Astropy Collaboration et al. 2022), photoutils (L. Bradley et al. 2023), scipy (P. Virtanen et al. 2020), IRAF (D. Tody 1986, 1993), SExtractor (E. Bertin & S. Arnouts 1996), PANHIT (K. Mawatari et al. 2020b), APLPy (T. Robitaille & E. Bressert 2012).

Appendix A
Observed Velocity Difference and Intrinsic Velocity Dispersion

To quantitatively examine the kinematic properties of COS-2987, we extracted 1D velocity and velocity dispersion profiles along a characteristic axis. We followed an approach applied to the KMOS^{3D} IFS data (E. Wisnioski et al. 2015). We first

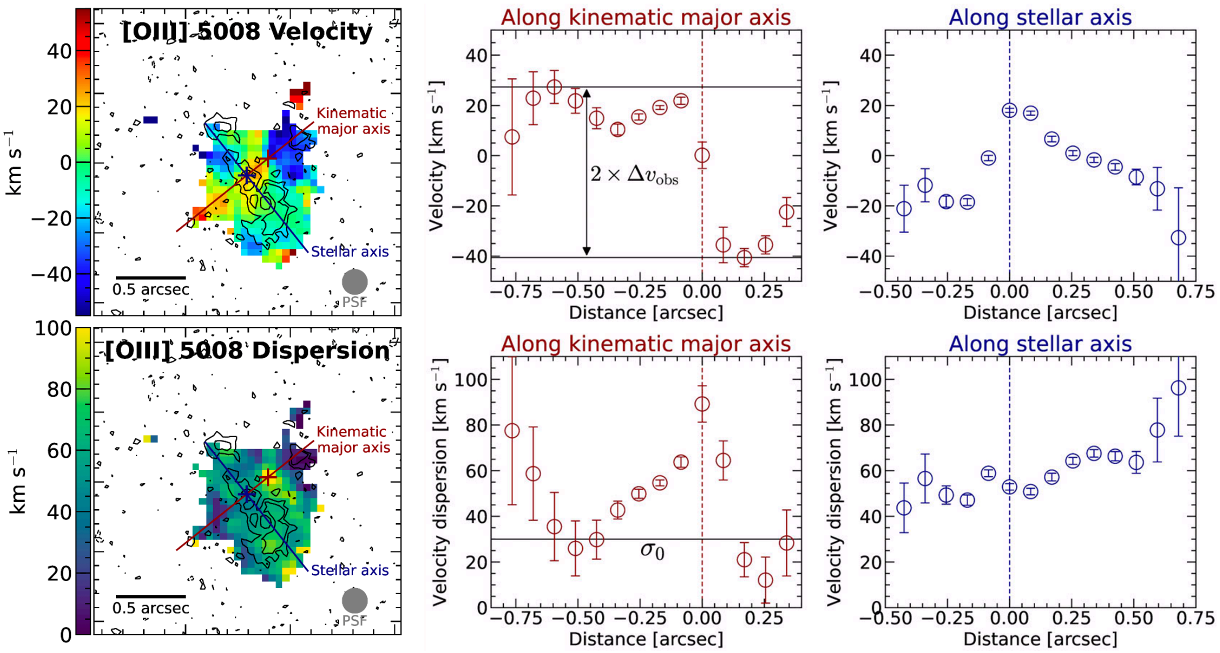

Figure 14. The top-left and bottom-left panels are the [O III] 5008 Å velocity and velocity dispersion maps, respectively. Each panel has 2″.2 × 2″.2 in size. The superposed brown (navy) line and plus sign correspond to the kinematic major (stellar) axis and its center. The PSF (FWHM) at the observed [O III] 5008 Å wavelength is shown by the gray filled circle at the bottom-right corner of each map. Contours show the F115W flux density at −2 (dashed), 2, and 4 × σ (solid). The top-middle (-right) and bottom-middle (-right) panels show the velocity and velocity dispersion profiles along the kinematic major (stellar) axis. The vertical dashed lines correspond to the center of the axes. The horizontal solid lines in the top-middle panel show the maximum and minimum velocities along the kinematic major axis, from which we calculated the observed velocity difference. The horizontal line in the bottom-middle panel shows the intrinsic velocity dispersion we measured.

determined the kinematic major axis on the 2D velocity map as the direction of the largest observed velocity difference. The kinematic center is defined as the spatial location of the velocity midpoint between the velocity extrema along the kinematic major axis. The kinematic major axis and center are shown in the velocity map of Figure 14 by the brown line and cross, respectively. The kinematic major axis passes through the sE, mN, and sN1 clumps. Along the kinematic major axis, we extracted 1D spectra from the NIRSpec cube data with apertures equivalent to the [O III] 5008 Å PSF, and performed the profile fit for the [O III] 5008 Å emission line in the same manner as in Section 3.1. From the line profile fit, the velocity and velocity dispersion were estimated, the latter of which was corrected for the instrumental spectral resolution ($\sigma_{\rm inst} \approx 48\,{\rm km\,s^{-1}}$). The obtained velocity and velocity dispersion profiles are shown in the top-middle and bottom-middle panels of Figure 14.

The velocity profile shows a dramatic change at the kinematic center from $v \sim +25\,{\rm km\,s^{-1}}$ (sE and mN) to $v \sim -40\,{\rm km\,s^{-1}}$ (sN1). The highest velocity dispersion is observed at the kinematic center. We measured an observed velocity difference and intrinsic velocity dispersion following E. Wisnioski et al. (2015). The observed velocity difference is defined by $\Delta v_{\rm obs} = (v_{\rm max} - v_{\rm min})/2$, where $v_{\rm max}$ and $v_{\rm min}$ are the maximum and minimal velocities in the velocity profile. This quantity is equivalent to the rotation velocity in the case of a rotating edge-on disk. For COS-2987, we measured $\Delta v_{\rm obs} = 34\,{\rm km\,s^{-1}}$. The intrinsic velocity dispersion, σ_0, is that measured at the outer regions typically along the kinematic major axis. This quantity is ideally free of resolved motions within the galaxy and the beam smearing effect. For COS-2987, it is difficult to determine σ_0 from the winding velocity dispersion profile. We roughly consider $\sigma_0 \sim 30\,{\rm km\,s^{-1}}$ (the bottom-middle panel of Figure 14).

We also investigated velocity and velocity dispersion profiles along the stellar mass distribution. We took an axis tracing the NIRCam F115W flux density distribution (i.e., distribution of young stars), which we refer to as the stellar axis (navy line on the velocity and velocity dispersion maps of Figure 14). We consider the intersection of the stellar and kinematic major axes as the stellar center for convenience. The velocity and velocity profiles measured along the stellar axis are shown in the top-right and bottom-right panels, respectively, of Figure 14. We can see a velocity gradient within the northern part (negative distances; mN) and gradual decrease from the northern (mN) to southern (mS) regions. The velocity dispersion gradually increases from mN to mS, which reflects the larger stellar mass in mS (Section 4.4).

Appendix B
PSF Matching

For the multiband SED analyses, we corrected the PSF difference among NIRSpec spectral data and NIRCam images. The NIRCam PSFs were generated by stacking point sources in each band image as described in Section 2.1. We generated NIRSpec PSF images at the wavelengths of the detected lines by averaging the cube data of the standard star 1808347 over a wavelength range within ±50 spectral elements (±0.033 μm) centered on each line. We further rotated the NIRSpec PSF images so as to correct for the difference in instrumental positional angle between the standard star and COS-2987. FWHMs of the NIRCam and NIRSpec PSFs range from 0″.06–0″.16 and 0″.16–0″.21, respectively.

Convolution kernels were created using `PyPHER` (A. Boucaud et al. 2016) so that all of the PSFs are homogenized to the NIRSpec Hα PSF with the largest FWHM = $0\farcs21$. To validate the accuracy of the kernels, we first convolved the PSF images. The convolved PSFs show good agreement within 10% precision for 2D images and within $0\farcs005$ for FWHMs.

We simply applied the kernel convolution to the eight NIRCam images. For NIRSpec, we constructed the PSF-matched data cube by convolving each spectral element slice image at wavelengths within $\pm 0.1\,\mu$m around the detected lines. We selected the convolution kernels whose wavelength is nearest from the given spectral element. We masked pixels whose wavelengths are more than 0.1 μm away from any lines. We again produced the line intensity maps by integrating the PSF-matched data cube over a wavelength range corresponding to 3× FWHM of each line profile measured in Section 3.1. All of the PSF-matched NIRCam images and NIRSpec line integrated intensity maps are shown in Figure 4.

ORCID iDs

Ken Mawatari https://orcid.org/0000-0003-4985-0201
Luca Costantin https://orcid.org/0000-0001-6820-0015
Takuya Hashimoto https://orcid.org/0000-0002-0898-4038
Javier Álvarez-Márquez https://orcid.org/0000-0002-7093-1877
Yuma Sugahara https://orcid.org/0000-0001-6958-7856
Luis Colina https://orcid.org/0000-0002-9090-4227
Akio K. Inoue https://orcid.org/0000-0002-7779-8677
Wataru Osone https://orcid.org/0009-0008-8424-100X
Santiago Arribas https://orcid.org/0000-0001-7997-1640
Rui Marques-Chaves https://orcid.org/0000-0001-8442-1846
Yurina Nakazato https://orcid.org/0000-0002-0984-7713
Masato Hagimoto https://orcid.org/0000-0001-8083-5814
Daniel Ceverino https://orcid.org/0000-0002-8680-248X
Naoki Yoshida https://orcid.org/0000-0001-7925-238X
Tom J. L. C. Bakx https://orcid.org/0000-0002-5268-2221
Yoshinobu Fudamoto https://orcid.org/0000-0001-7440-8832
Alejandro Crespo Gómez https://orcid.org/0000-0003-2119-277X
Hiroshi Matsuo https://orcid.org/0000-0003-3278-2484
Miguel Pereira-Santaella https://orcid.org/0000-0002-4005-9619
Carmen Blanco-Prieto https://orcid.org/0009-0005-5448-5239
Yi W. Ren https://orcid.org/0000-0002-6510-5028
Yoichi Tamura https://orcid.org/0000-0003-4807-8117

References

Aihara, H., AlSayyad, Y., Ando, M., et al. 2019, PASJ, 71, 114
Akhlaghi, M., & Ichikawa, T. 2015, ApJS, 220, 1
Álvarez-Márquez, J., Burgarella, D., Buat, V., Ilbert, O., & Pérez-González, P. G. 2019, A&A, 630, A153
Álvarez-Márquez, J., Burgarella, D., Heinis, S., et al. 2016, A&A, 587, A122
Álvarez-Márquez, J., Colina, L., Crespo Gómez, A., et al. 2024, A&A, 686, A85
Álvarez-Márquez, J., Crespo Gómez, A., Colina, L., et al. 2025, A&A, 695, A250
Álvarez-Márquez, J., Hashimoto, T., Arribas, S., et al. 2021, ALMA [OIII] 88um Emitters. Signpost of Early Stellar Buildup and Reionization in the Universe, JWST Proposal. Cycle 1, ID. #1840,
Arribas, S., Perna, M., Rodríguez Del Pino, B., et al. 2024, A&A, 688, A146
Asada, Y., Sawicki, M., Abraham, R., et al. 2024, MNRAS, 527, 11372
Astropy Collaboration, Price-Whelan, A. M., Lim, P. L., et al. 2022, ApJ, 935, 167
Atek, H., Furtak, L. J., Oesch, P., et al. 2022, MNRAS, 511, 4464
Atek, H., Labbé, I., Furtak, L. J., et al. 2024, Natur, 626, 975
Bagley, M. B., Finkelstein, S. L., Koekemoer, A. M., et al. 2023, ApJL, 946, L12
Bakx, T. J. L. C., Tamura, Y., Hashimoto, T., et al. 2020, MNRAS, 493, 4294
Barnes, J. E., & Hernquist, L. 1996, ApJ, 471, 115
Belitsky, V., Bylund, M., Desmaris, V., et al. 2018, A&A, 611, A98
Bertin, E., & Arnouts, S. 1996, A&AS, 117, 393
Böker, T., Beck, T. L., Birkmann, S. M., et al. 2023, PASP, 135, 038001
Boucaud, A., Bocchio, M., Abergel, A., et al. 2016, A&A, 596, A63
Bouwens, R. J., Aravena, M., Decarli, R., et al. 2016a, ApJ, 833, 72
Bouwens, R. J., Smit, R., Labbé, I., et al. 2016b, ApJ, 831, 176
Bowler, R. A. A., Cullen, F., McLure, R. J., Dunlop, J. S., & Avison, A. 2022, MNRAS, 510, 5088
Bowler, R. A. A., Inami, H., Sommovigo, L., et al. 2024, MNRAS, 527, 5808
Boyett, K., Bunker, A. J., Curtis-Lake, E., et al. 2024, MNRAS, 535, 1796
Bradley, L., Sipőcz, B., Robitaille, T., et al. 2023, astropy/photutils: v1.10.0, Zenodo, doi:10.5281/zenodo.1035865
Bruzual, G., & Charlot, S. 2003, MNRAS, 344, 1000
Bushouse, H., Eisenhamer, J., Dencheva, N., et al. 2022, spacetelescope/jwst: JWST v1.6.2, Zenodo, doi:10.5281/zenodo.6984366
Calzetti, D. 2001, PASP, 113, 1449
Calzetti, D. 2013, in Secular Evolution of Galaxies, ed. J. Falcón-Barroso & J. H. Knapen (Cambridge: Cambridge Univ. Press), 419
Calzetti, D., Armus, L., Bohlin, R. C., et al. 2000, ApJ, 533, 682
Cameron, A. J., Saxena, A., Bunker, A. J., et al. 2023, A&A, 677, A115
CASA Team, Bean, B., Bhatnagar, S., et al. 2022, PASP, 134, 114501
Ceverino, D., Dekel, A., & Bournaud, F. 2010, MNRAS, 404, 2151
Ceverino, D., Glover, S. C. O., & Klessen, R. S. 2017, MNRAS, 470, 2791
Ceverino, D., Klessen, R. S., & Glover, S. C. O. 2019, MNRAS, 484, 1366
Chabrier, G. 2003, PASP, 115, 763
Chen, Z., Stark, D. P., Endsley, R., et al. 2023, MNRAS, 518, 5607
Choustikov, N., Katz, H., Saxena, A., et al. 2024, MNRAS, 529, 3751
Cole, J. W., Papovich, C., Finkelstein, S. L., et al. 2025, ApJ, 979, 193
Conselice, C. J., Yang, C., & Bluck, A. F. L. 2009, MNRAS, 394, 1956
Contini, T., Garilli, B., Le Fèvre, O., et al. 2012, A&A, 539, A91
Costantin, L., Pérez-González, P. G., Guo, Y., et al. 2023, Natur, 623, 499
Cox, T. J., Di Matteo, T., Hernquist, L., et al. 2006, ApJ, 643, 692
da Cunha, E., Groves, B., Walter, F., et al. 2013, ApJ, 766, 13
Dekel, A., & Krumholz, M. R. 2013, MNRAS, 432, 455
Dekel, A., Sari, R., & Ceverino, D. 2009, ApJ, 703, 785
Di Matteo, P., Bournaud, F., Martig, M., et al. 2008, A&A, 492, 31
Di Matteo, P., Combes, F., Melchior, A. L., & Semelin, B. 2007, A&A, 468, 61
Di Teodoro, E. M., & Fraternali, F. 2015, MNRAS, 451, 3021
Draine, B. T. 2011, Physics of the Interstellar and Intergalactic Medium (Princeton, NJ: Princeton Univ. Press)
Drake, A. B., Garel, T., Wisotzki, L., et al. 2017, A&A, 608, A6
Duan, Q., Conselice, C. J., Li, Q., et al. 2025, MNRAS, 540, 774
Dunlop, J. S., Abraham, R. G., Ashby, M. L. N., et al. 2021, PRIMER: Public Release IMaging for Extragalactic Research, JWST Proposal. Cycle 1, ID. #1837,
Ediss, G. A., Carter, M., Cheng, J., et al. 2004, in Fifteenth Int. Symp. Space Terahertz Technology, ed. G. Narayanan, 181
Endsley, R., Chisholm, J., Stark, D. P., Topping, M. W., & Whitler, L. 2025, ApJ, 987, 189
Erb, D. K., Steidel, C. C., Shapley, A. E., et al. 2006, ApJ, 647, 128
Faisst, A. L., Capak, P. L., Yan, L., et al. 2017, ApJ, 847, 21
Fakhouri, O., & Ma, C.-P. 2008, MNRAS, 386, 577
Fazio, G. G., Hora, J. L., Allen, L. E., et al. 2004, ApJS, 154, 10
Fensch, J., Renaud, F., Bournaud, F., et al. 2017, MNRAS, 465, 1934
Finkelstein, S. L., Bagley, M. B., Arrabal Haro, P., et al. 2022, ApJL, 940, L55
Finkelstein, S. L., Bagley, M. B., Arrabal Haro, P., et al. 2025, ApJL, 983, L4
Forbes, J. C., Krumholz, M. R., Burkert, A., & Dekel, A. 2014, MNRAS, 438, 1552
Förster Schreiber, N. M., Genzel, R., Bouché, N., et al. 2009, ApJ, 706, 1364
Förster Schreiber, N. M., Genzel, R., Newman, S. F., et al. 2014, ApJ, 787, 38
Förster Schreiber, N. M., Renzini, A., Mancini, C., et al. 2018, ApJS, 238, 21
Förster Schreiber, N. M., Übler, H., Davies, R. L., et al. 2019, ApJ, 875, 21
Fudamoto, Y., Oesch, P. A., Faisst, A., et al. 2020, A&A, 643, A4
Fudamoto, Y., Oesch, P. A., Schinnerer, E., et al. 2017, MNRAS, 472, 483
Fudamoto, Y., Smit, R., Bowler, R. A. A., et al. 2022, ApJ, 934, 144
Fujimoto, S., Arrabal Haro, P., Dickinson, M., et al. 2023, ApJL, 949, L25
Fujimoto, S., Ouchi, M., Kohno, K., et al. 2025, NatAs, 9, 1553

Furusawa, H., Koike, M., Takata, T., et al. 2018, PASJ, 70, S3

Gaia Collaboration, Prusti, T., de Bruijne, J. H. J., et al. 2016, A&A, 595, A1

Gardner, J. P., Mather, J. C., Abbott, R., et al. 2023, PASP, 135, 068001

Genzel, R., Burkert, A., Bouché, N., et al. 2008, ApJ, 687, 59

Genzel, R., Tacconi, L. J., Eisenhauer, F., et al. 2006, Natur, 442, 786

Giménez-Arteaga, C., Fujimoto, S., Valentino, F., et al. 2024, A&A, 686, A63

Gnerucci, A., Marconi, A., Cresci, G., et al. 2011, A&A, 528, A88

Golini, G., Montes, M., Carrasco, E. R., Román, J., & Trujillo, I. 2024, A&A, 684, A99

Gordon, K. D., Clayton, G. C., Misselt, K. A., Landolt, A. U., & Wolff, M. J. 2003, ApJ, 594, 279

Grogin, N. A., Kocevski, D. D., Faber, S. M., et al. 2011, ApJS, 197, 35

Guo, Y., Ferguson, H. C., Bell, E. F., et al. 2015, ApJ, 800, 39

Harikane, Y., Inoue, A. K., Ellis, R. S., et al. 2025, ApJ, 980, 138

Hashimoto, T., Álvarez-Márquez, J., Fudamoto, Y., et al. 2023a, ApJL, 955, L2

Hashimoto, T., Inoue, A. K., Mawatari, K., et al. 2019, PASJ, 71, 71

Hashimoto, T., Inoue, A. K., Sugahara, Y., et al. 2023b, ApJ, 952, 48

Hashimoto, T., Laporte, N., Mawatari, K., et al. 2018, Natur, 557, 392

Hirschmann, M., Charlot, S., & Somerville, R. S. 2023, MNRAS, 526, 3504

Hsiao, T. Y.-Y., Álvarez-Márquez, J., Coe, D., et al. 2024, ApJ, 973, 81

Hu, W., Papovich, C., Shen, L., et al. 2025, NatAs, 9, 1568

Inoue, A. K. 2011, MNRAS, 415, 2920

Inoue, A. K., Shimizu, I., Iwata, I., & Tanaka, M. 2014a, MNRAS, 442, 1805

Inoue, A. K., Shimizu, I., Tamura, Y., et al. 2014b, ApJL, 780, L18

Inoue, S., Dekel, A., Mandelker, N., et al. 2016, MNRAS, 456, 2052

Jakobsen, P., Ferruit, P., Alves de Oliveira, C., et al. 2022, A&A, 661, A80

JDADF Developers, Averbukh, J., Bradley, L., et al., 2023 Jdaviz: JWST astronomical data analysis tools in the Jupyter platform, Astrophysics Source Code Library, ascl:2307.001

Jones, G. C., Bowler, R., Bunker, A. J., et al. 2024a, arXiv:2412.15027

Jones, G. C., Bunker, A. J., Telikova, K., et al. 2025, MNRAS, 540, 3311

Jones, G. C., Übler, H., Perna, M., et al. 2024b, A&A, 682, A122

Jung, I., Finkelstein, S. L., Arrabal Haro, P., et al. 2024, ApJ, 967, 73

Kashino, D., Silverman, J. D., Rodighiero, G., et al. 2013, ApJL, 777, L8

Kawanomoto, S., Uraguchi, F., Komiyama, Y., et al. 2018, PASJ, 70, 66

Kennicutt, R. C., & Evans, N. J. 2012, ARA&A, 50, 531

Kewley, L. J., & Dopita, M. A. 2002, ApJS, 142, 35

Koekemoer, A. M., Faber, S. M., Ferguson, H. C., et al. 2011, ApJS, 197, 36

Kohandel, M., Pallottini, A., Ferrara, A., et al. 2024, A&A, 685, A72

Komiyama, Y., Obuchi, Y., Nakaya, H., et al. 2018, PASJ, 70, S2

Kramida, A., Ralchenko, Y., Reader, J. & NIST ASD Team 2020, NIST Atomic Spectra Database (ver. 5.8), [Online]. Available: https://physics.nist.gov/asd [2020, December 21]. National Institute of Standards and Technology, Gaithersburg, MD

Kreckel, K., Groves, B., Schinnerer, E., et al. 2013, ApJ, 771, 62

Krumholz, M., & Burkert, A. 2010, ApJ, 724, 895

Lang, P., Förster Schreiber, N. M., Genzel, R., et al. 2017, ApJ, 840, 92

Laporte, N., Nakajima, K., Ellis, R. S., et al. 2017, ApJ, 851, 40

Laseter, I. H., Maseda, M. V., Curti, M., et al. 2024, A&A, 681, A70

Law, D. R., Steidel, C. C., Erb, D. K., et al. 2009, ApJ, 697, 2057

Levesque, E. M., & Leitherer, C. 2013, ApJ, 779, 170

Lotz, J. M., Jonsson, P., Cox, T. J., & Primack, J. R. 2010, MNRAS, 404, 575

Luridiana, V., Morisset, C., & Shaw, R. A. 2015, A&A, 573, A42

Mandelker, N., Dekel, A., Ceverino, D., et al. 2017, MNRAS, 464, 635

Marconcini, C., D'Eugenio, F., Maiolino, R., et al. 2024, MNRAS, 533, 2488

Marshall, M. A., Perna, M., Willott, C. J., et al. 2023, A&A, 678, A191

Matthee, J., Mackenzie, R., Simcoe, R. A., et al. 2023, ApJ, 950, 67

Matthee, J., Sobral, D., Best, P., et al. 2017, MNRAS, 465, 3637

Mawatari, K., Inoue, A. K., Hashimoto, T., et al. 2020a, ApJ, 889, 137

Mawatari, K., Inoue, A. K., Yamanaka, S., Hashimoto, T., & Tamura, Y. 2020b, IAUS, 341, 285

McLure, R. J., Dunlop, J. S., Cullen, F., et al. 2018, MNRAS, 476, 3991

McMullin, J. P., Waters, B., Schiebel, D., Young, W., & Golap, K. 2007, ASPC, 376, 127

Meurer, G. R., Heckman, T. M., & Calzetti, D. 1999, ApJ, 521, 64

Mihos, J. C., & Hernquist, L. 1994, ApJL, 425, L13

Mihos, J. C., & Hernquist, L. 1996, ApJ, 464, 641

Miyazaki, S., Komiyama, Y., Kawanomoto, S., et al. 2018, PASJ, 70, S1

Morishita, T., Roberts-Borsani, G., Treu, T., et al. 2023, ApJL, 947, L24

Morishita, T., Stiavelli, M., Chary, R.-R., et al. 2024a, ApJ, 963, 9

Morishita, T., Stiavelli, M., Grillo, C., et al. 2024b, ApJ, 971, 43

Nakajima, K., & Ouchi, M. 2014, MNRAS, 442, 900

Nakajima, K., Ouchi, M., Isobe, Y., et al. 2023, ApJS, 269, 33

Nakazato, Y., Ceverino, D., & Yoshida, N. 2024, ApJ, 975, 238

Nayyeri, H., Hemmati, S., Mobasher, B., et al. 2017, ApJS, 228, 7

Neeleman, M., Prochaska, J. X., Kanekar, N., & Rafelski, M. 2020, Natur, 581, 269

Nelson, E. J., van Dokkum, P. G., Momcheva, I. G., et al. 2016, ApJL, 817, L9

Newman, S. F., Genzel, R., Förster Schreiber, N. M., et al. 2013, ApJ, 767, 104

Osterbrock, D. E., & Ferland, G. J. 2006, Astrophysics of Gaseous Nebulae and Active Galactic Nuclei (Sausalito, CA: University Science Books)

Ota, K., Walter, F., Ohta, K., et al. 2014, ApJ, 792, 34

Parlanti, E., Carniani, S., Pallottini, A., et al. 2023, A&A, 673, A153

Parlanti, E., Carniani, S., Übler, H., et al. 2024, A&A, 684, A24

Pérez-González, P. G., Costantin, L., Langeroodi, D., et al. 2023, ApJL, 951, L1

Pérez-González, P. G., Östlin, G., Costantin, L., et al. 2025, ApJ, 991, 179

Perna, M., Arribas, S., Marshall, M., et al. 2023, A&A, 679, A89

Posses, A. C., Aravena, M., González-López, J., et al. 2023, A&A, 669, A46

Prevot, M. L., Lequeux, J., Maurice, E., Prevot, L., & Rocca-Volmerange, B. 1984, A&A, 132, 389

Prochaska, J. X., Tejos, N., Crighton, N., et al. 2017, Linetools/Linetools: Third Minor Release, v0.3, Zenodo, doi:10.5281/zenodo.1036773

Reddy, N. A., Kriek, M., Shapley, A. E., et al. 2015, ApJ, 806, 259

Reddy, N. A., Oesch, P. A., Bouwens, R. J., et al. 2018, ApJ, 853, 56

Ren, Y. W., Inoue, A. K., Álvarez-Márquez, J., et al. 2025, MNRAS, 544, 4722

Renaud, F., Bournaud, F., Kraljic, K., & Duc, P. A. 2014, MNRAS, 442, L33

Rigby, J., Perrin, M., McElwain, M., et al. 2023, PASP, 135, 048001

Rizzo, F., Bacchini, C., Kohandel, M., et al. 2024, A&A, 689, A273

Rizzo, F., Kohandel, M., Pallottini, A., et al. 2022, A&A, 667, A5

Rizzo, F., Vegetti, S., Powell, D., et al. 2020, Natur, 584, 201

Robertson, B. E., Furlanetto, S. R., Schneider, E., et al. 2013, ApJ, 768, 71

Robitaille, T., & Bressert, E., 2012 APLpy: Astronomical Plotting Library in Python, Astrophysics Source Code Library, ascl:1208.017

Rodrigues, M., Hammer, F., Flores, H., Puech, M., & Athanassoula, E. 2017, MNRAS, 465, 1157

Rodriguez-Gomez, V., Genel, S., Vogelsberger, M., et al. 2015, MNRAS, 449, 49

Romeo, A. B., & Agertz, O. 2014, MNRAS, 442, 1230

Romeo, A. B., Burkert, A., & Agertz, O. 2010, MNRAS, 407, 1223

Salmon, B., Papovich, C., Finkelstein, S. L., et al. 2015, ApJ, 799, 183

Saxena, A., Bunker, A. J., Jones, G. C., et al. 2024, A&A, 684, A84

Scholtz, J., Curti, M., D'Eugenio, F., et al. 2025, MNRAS, 539, 2463

Scoville, N., Faisst, A., Capak, P., et al. 2015, ApJ, 800, 108

Sekimoto, Y., Iizuko, Y., Satou, N., et al. 2008, in Ninteenth Int. Symp. Space Terahertz Technology, ed. W. Wild, 253

Shapley, A. E., Sanders, R. L., Reddy, N. A., Topping, M. W., & Brammer, G. B. 2023, ApJ, 954, 157

Shibuya, T., Ouchi, M., Kubo, M., & Harikane, Y. 2016, ApJ, 821, 72

Shibuya, T., Ito, Y., Asai, K., et al. 2025, PASJ, 77, 21

Simons, R. C., Kassin, S. A., Trump, J. R., et al. 2016, ApJ, 830, 14

Smit, R., Bouwens, R. J., Carniani, S., et al. 2018, Natur, 553, 178

Smit, R., Bouwens, R. J., Franx, M., et al. 2015, ApJ, 801, 122

Sommovigo, L., Ferrara, A., Carniani, S., et al. 2022a, MNRAS, 517, 5930

Sommovigo, L., Ferrara, A., Pallottini, A., et al. 2022b, MNRAS, 513, 3122

Sparre, M., Hayward, C. C., Feldmann, R., et al. 2017, MNRAS, 466, 88

Speagle, J. S., Steinhardt, C. L., Capak, P. L., & Silverman, J. D. 2014, ApJS, 214, 15

Steidel, C. C., Rudie, G. C., Strom, A. L., et al. 2014, ApJ, 795, 165

Steidel, C. C., Strom, A. L., Pettini, M., et al. 2016, ApJ, 826, 159

Storey, P. J., & Hummer, D. G. 1995, MNRAS, 272, 41

Storey, P. J., & Zeippen, C. J. 2000, MNRAS, 312, 813

Stott, J. P., Swinbank, A. M., Johnson, H. L., et al. 2016, MNRAS, 457, 1888

Sugahara, Y., Álvarez-Márquez, J., Hashimoto, T., et al. 2025, ApJ, 981, 135

Tamura, Y., Bakx, T. J. L. C., Inoue, A. K., et al. 2023, ApJ, 952, 9

Tamura, Y., Mawatari, K., Hashimoto, T., et al. 2019, ApJ, 874, 27

Tang, M., Stark, D. P., Chen, Z., et al. 2023, MNRAS, 526, 1657

Teague, R., & Foreman-Mackey, D. 2018, RNAAS, 2, 173

Telikova, K., González-López, J., Aravena, M., et al. 2025, A&A, 699, A5

Telles, E., & Melnick, J. 2018, A&A, 615, A55

Theios, R. L., Steidel, C. C., Strom, A. L., et al. 2019, ApJ, 871, 128

Tody, D. 1986, SPIE, 627, 733

Tody, D. 1993, ASPC, 52, 173

Tokuoka, T., Inoue, A. K., Hashimoto, T., et al. 2022, ApJL, 933, L19

Tsukui, T., & Iguchi, S. 2021, Sci, 372, 1201

Übler, H., Genzel, R., Wisnioski, E., et al. 2019, ApJ, 880, 48

Übler, H., Maiolino, R., Curtis-Lake, E., et al. 2023, A&A, 677, A145

Umehata, H., Steidel, C. C., Smail, I., et al. 2025, PASJ, 77, 432

Usui, M., Mawatari, K., Álvarez-Márquez, J., et al. 2025, ApJL, 991, L38

Venturi, G., Carniani, S., Parlanti, E., et al. 2024, A&A, 691, A19
Virtanen, P., Gommers, R., Oliphant, T. E., et al. 2020, NatMe, 17, 261
Weaver, J. R., Kauffmann, O. B., Ilbert, O., et al. 2022, ApJS, 258, 11
Weisz, D. R., Johnson, B. D., Johnson, L. C., et al. 2012, ApJ, 744, 44
Welch, B., Olivier, G. M., Hutchison, T. A., et al. 2024, ApJ, 975, 196
Wisnioski, E., Förster Schreiber, N. M., Fossati, M., et al. 2019, ApJ, 886, 124
Wisnioski, E., Förster Schreiber, N. M., Wuyts, S., et al. 2015, ApJ, 799, 209
Witstok, J., Smit, R., Maiolino, R., et al. 2022, MNRAS, 515, 1751
Wootten, A., & Thompson, A. R. 2009, IEEEP, 97, 1463
Xu, Y., Ouchi, M., Yajima, H., et al. 2024, ApJ, 976, 142
Zavala, J. A., Castellano, M., Akins, H. B., et al. 2025, NatAs, 9, 155